# Distribution of Velocity Gradient Orientations: Mapping Magnetization with the Velocity Gradient Technique

A. Lazarian<sup>1</sup>, Ka Ho Yuen<sup>1</sup>, Ka Wai Ho<sup>2</sup>, Junda Chen<sup>1</sup>, Victor Lazarian<sup>1</sup>, Zekun Lu<sup>1,3</sup>, Bo Yang<sup>1</sup>, and Yue Hu<sup>1,4</sup>

Department of Astronomy, University of Wisconsin-Madison, Madison, WI, USA; lazarian@astro.wisc.edu

Department of Physics, The Chinese University of Hong Kong, Hong Kong

School of Astronomy and Space Science, Nanjing University, Nanjing, People's Republic of China

College of Electronics and Information Engineering, Tongji University, Shanghai, People's Republic of China

Received 2018 April 7; revised 2018 July 31; accepted 2018 August 1; published 2018 September 19

### **Abstract**

Recent developments of the velocity gradient technique (VGT) show that the velocity gradients provide a reliable tracing of the magnetic field direction in turbulent plasmas. In this paper, we explore the ability of velocity gradients to measure the magnetization of the interstellar medium. We demonstrate that the distribution of velocity gradient orientations provides a reliable estimation of the magnetization of the media. In particular, we determine the relation between Alfvénic Mach number  $M_A$  in the range of  $M_A \in [0.2, 1.7]$  and properties of the velocity gradient distribution, namely, with the dispersion of velocity gradient orientation as well as with the peak-to-base ratio of the amplitudes. We apply our technique to a selected GALFA-HI region and find the results consistent with the expected behavior of  $M_A$ . Using 3D magnetohydrodynamic simulations, we successfully compare the results with our new measure of magnetization that is based on the dispersion of starlight polarization. We demonstrate that combined with the velocity dispersion along the line-of-sight direction, our technique is capable of delivering the magnetic field strength. The new technique opens a way to measure magnetization using other gradient measures, such as synchrotron intensity gradients and synchrotron polarization gradients.

Key words: ISM: general - ISM: structure - magnetohydrodynamics (MHD) - radio continuum: ISM - turbulence

### 1. Introduction

Diffuse interstellar media and molecular clouds are both turbulent and magnetized (Larson 1981; Elmegreen & Scalo 2004; Mac Low & Klessen 2004; Ballesteros-Paredes et al. 2007; McKee & Ostriker 2007; Chepurnov & Lazarian 2009). Magnetization of the media is extremely important for understanding key astrophysical problems, e.g., the problem of star formation (Mestel & Spitzer 1956; Schmidt 1959; Mouschovias & Spitzer 1976; Shu 1977, 1992; Koenigl 1991; Shu et al. 1994; Kennicutt 1998a, 1998b; Chapman et al. 2013; Hull et al. 2013; Burkhart et al. 2015; Burkhart 2018) and cosmic ray propagation and acceleration (Fermi 1949; Ginzburg & Syrovatskii 1964; Parker 1965, 1979; Jokipii 1966; Bell 1978; Caprioli & Spitkovsky 2014).

Various techniques have been proposed to study the magnetization of the interstellar media (Draine 2011). Magnetic field strength and structures can be measured by both direct or indirect approaches. Spectral line splitting due to the Zeeman effect provides a direct measurement of the line-of-sight (LOS) component of the magnetic field strength (Goodman et al. 1989; Heiles et al. 1993; Crutcher 1999, 2010; Crutcher et al. 1999; Bourke et al. 2001; Falgarone et al. 2008), but the method is mostly applied to targets at lower Galactic latitude (Crutcher 2012) and does not provide an insight into the total magnetization or the magnetic field directions perpendicular to the LOS unless the two circular polarization components are both resolved (Crutcher 2007). Polarized dust emission (Cudlip et al. 1982; Hildebrand et al. 1984, 2000; Dragovan 1986; Hildebrand 1988; Novak et al. 1997; Holland et al. 1999; Vaillancourt & Matthews 2012) as well as measuring the starlight polarization arising from aligned dust (Clemens et al. 2012a, 2012b, 2013; Andersson et al. 2015) provides the main indirect method of mapping the plane-of-sky magnetic field strength using the Davis-Chandrasekhar-Fermi method (CF; Davis 1951; Chandrasekhar

& Fermi 1953; Falceta-Gonçalves et al. 2008; Hildebrand et al. 2009; Houde et al. 2009, 2011, 2016; Chitsazzadeh et al. 2012), but the estimation of magnetic field strength using the CF method can be significantly different from the true value even in synthetic maps obtained with magnetohydrodynamic (MHD) simulations for the case of trans-Alfvénic turbulence (Falceta-Gonçalves et al. 2008; Cho & Yoo 2016).

Anisotropies of magnetized turbulence (see Brandenburg & Lazarian 2013 for a review of the theory) provides an alternative way for studying magnetic field directions. Lazarian et al. (2002) demonstrated that using the correlation functions of intensities in velocity channel maps,<sup>5</sup> it is possible to study the magnetic field directions. Further development of the technique showed that the the correlation function anisotropy (CFA; see also Appendix B) is a promising way to study both magnetic field direction and media magnetization, and also to distinguish the contributions from Alfvén, slow, and fast modes (see Esquivel et al. 2015; Kandel et al. 2016, 2017a). The CFA technique shows effective results on both the channel maps and velocity centroids (Esquivel & Lazarian 2005; Kandel et al. 2017b). The CFA is also applicable to the study of magnetic fields and turbulence properties with synchrotron intensity and polarization fluctuations (Lazarian & Pogosyan 2012, 2016).

The approach in Lazarian et al. (2002) can be realized in different ways, with the CFA being its particular realization. For instance, the anisotropies can be studied by employing the principal component analysis technique as described in Heyer et al. (2008). Our study in Yuen et al. (2018a) showed, however, that there are no particular advantages of this technique compared to

<sup>&</sup>lt;sup>5</sup> Intensity fluctuations within "thin" (see Section 3) velocity channel maps are in most cases dominated by velocity fluctuations (Lazarian & Pogosyan 2000, 2004).

either the velocity gradient technique (VGT) or CFA. Therefore we do not discuss this technique further in this paper.

A different approach of magnetic field tracing with gradients of observable measures (e.g., velocity centroids, synchrotron intensity, and synchrotron polarization) has been suggested recently (González-Casanova & Lazarian 2017; Lazarian et al. 2017; Yuen & Lazarian 2017a, 2017b; Lazarian & Yuen 2018a, 2018b). This technique in terms of theoretical justification is related to the CFA. It is known that MHD fluctuations can be decomposed into fundamental Alfvén, fast, and slow modes (Biskamp 2003; see Appendix A). A numerical study in Cho & Lazarian (2003) testifies that the three modes are evolving and create their own cascades, with Alfvén and slow modes showing significant anisotropy along the magnetic field direction. With the contribution of Alfvén and slow modes being dominant, especially in the weakly compressible cases (Lithwick & Goldreich 2001; Cho & Lazarian 2002), a prominent anisotropy is both expected and observed in the MHD turbulence, and it contains all the three MHD modes (see Cho & Lazarian 2003, Kowal & Lazarian 2010). The corresponding elongation of turbulent fluctuations causes the velocity correlations to be stronger along the local magnetic field direction. At the same time, the velocity gradients become perpendicular to magnetic field. As a result, one can estimate the direction of magnetic field by the direction of the velocity gradients through a 90° rotation on the local gradient direction. Similarly, one can infer the direction of the magnetic fields by rotating the the magnetic gradients by 90°. The latter can be revealed through studying synchrotron intensity and synchrotron polarization gradients (SPGs). For the sake of simplicity, within this study we focus on velocity gradients. However, in view of the symmetric way in which velocity and magnetic fluctuations enter Alfvénic turbulence, all our results in this paper are also applicable to magnetic field gradients.

Density fluctuations for a low sonic Mach number  $M_s$  will follow the velocity statistics. Thus for low  $M_s$ , density gradients behave similarly to velocity gradients. However, density is not always a passive scalar of velocity information, and the density gradients created by shocks tend to be parallel to magnetic field in the case of high  $M_s$ . Therefore a combination of density and velocity gradients provides a better insight into the properties of turbulence in diffuse media.

In Alfvénic turbulence the directions of k vectors of turbulent velocities have a statistical distribution (see GS95; Cho et al. 2002a). Similarly, the gradients also have a distribution of directions, with the most probable orientation of gradients being perpendicular to the magnetic field direction. To find this most probably orientation, in practical studies, the velocity gradients are calculated over a block of data points. When the statistics is sufficiently rich, the histogram of gradient orientations within a block becomes Gaussian, with the peak of the Gaussian corresponding to the local direction of the magnetic field within the block.<sup>6</sup>

In our earlier studies (e.g., Yuen & Lazarian 2017a; Lazarian & Yuen 2018a) we demonstrated that the peak of the

distribution is correlated with the magnetic field direction, and this provides a promising way of magnetic field studies, including studies of the 3D distribution of magnetic fields. Our earlier studies were focused on magnetic field tracing by determining the peak of the Gaussian distribution of gradients (see Lazarian et al. 2017; Yuen & Lazarian 2017a, 2017b; Lazarian & Yuen 2018a, 2018b). However, it became clear that the distribution of gradient orientations<sup>8</sup> is also an informative measure. For instance, the dispersion of the gradient orientation distribution was used to identify the regions of collapse induced by self-gravity (Lazarian & Yuen 2018a). However, gravitational collapse is a special case when the properties of the turbulent flow change dramatically. In this paper we focus our attention on the properties of the distribution of gradient orientations for magnetized turbulence in diffuse regions where the effects of self-gravity is negligible. We show that for such settings the properties of the distribution of gradient orientations is directly related to the Alfvén Mach number  $M_A$ , which is the ratio of the turbulent velocity  $V_L$  at the scale  $L_{\rm inj}$  and the media Alfvén velocity  $V_A$ . We also demonstrate the ways of using spectroscopic data in order to convert the distribution of  $M_{\rm A}$  into the distribution of magnetic field strengths.

In a companion paper by Yuen et al. (2018b), we found that the amplitude of velocity gradients can be used to study the sonic  $M_s = V_L/c_s$ , where  $c_s$  is the sound speed. Thus the two most important measures of turbulence,  $M_A$  and  $M_s$  can be obtained using the gradient techniques.

In this paper, we focus on the relation of the velocity gradient dispersion to  $M_A$ , and thus provide a way to map the magnetization in the media. In what follows, we provide the theoretical justification of this work in Section 2, discuss numerical simulations that we employ to test our expectations in Section 3, and analyze our results in Section 4, including an application to observations in Section 4.5. We briefly discuss the ways of obtaining the magnetic field strength using our estimation of  $M_A$  in Section 5. Our discussion and summary are provided in Sections 6 and 7, respectively.

### 2. Theoretical Considerations

In what follows, we consider velocity fluctuations arising from MHD turbulence. Similar considerations, however, are applicable to the fluctuations of a turbulent magnetic field.

### 2.1. Basic MHD Turbulence Considerations

The predictive theory of incompressible MHD turbulence was formulated in Goldreich & Sridhar (1995, hereafter GS95). This theory can be understood on the basis of the Kolmogorov hydrodynamic turbulence theory if a concept of fast turbulent reconnection (Lazarian & Vishniac 1999, hereafter LV99) is added. Indeed, according to LV99, magnetic reconnection occurs in just one eddy turnover time for eddies at all scales. Therefore,

<sup>&</sup>lt;sup>6</sup> This procedure should not be confused with the technique called histogram of relative orientations (HRO) that was explored by Soler et al. (2013) for the intensity gradients (IGs). The latter requires polarimetry data to define the direction of the magnetic field and draws the relative orientation of the polarization directions and the IGs as a function of column density. Our technique is polarization independent and is the way of finding the magnetic field direction, which is different from the purpose of the HRO. We stress that our approach, when applied to velocities and densities, provides the spatial direction of the magnetic field, while the HRO provides the correlation of the relative orientation of the IGs as a function of column density (see more comparisons in YL17b, LY18a).

The 3D studies are possible with the velocity channel gradients (VChGs) using the galactic rotation curve to distinguish different emitting regions (Lazarian & Yuen 2018a). Another way of obtaining the 3D magnetic field structure employs the Faraday depolarization within the SPG studies (Lazarian & Yuen 2018b).

 $<sup>^8</sup>$  Similar to polarization, the gradients have and ambiguity of  $180^{\rm o}$  in determining the actual direction of the magnetic field.

In the regions of self-gravitational collapse, the relative direction of velocity gradients and magnetic field changes gradually from perpendicular to parallel. This induces an increase of the dispersion (Yuen & Lazarian 2017b; Lazarian & Yuen 2018a).

motions that mix magnetic field lines perpendicular to their direction is the way in which the turbulent cascade does not need to bend magnetic field lines and therefore encounters the least resistance from the field. As a result, the turbulent eddies are elongated along the direction of the magnetic field. Incidentally, this justifies the concept of alignment of turbulent eddies with the local magnetic field direction that was not a part of the original GS95 picture<sup>10</sup>, but the necessity of using the local frame of reference was pointed out by numerical simulations (see Cho & Vishniac 2000; Maron & Goldreich 2001).

The modern theory of MHD turbulence is discussed in, e.g., Brandenburg & Lazarian (2013). Here we briefly summarize the points that are essential for understanding the properties of gradients (see also Appendix A). As we explain in Appendix A, the properties of Alfvénic modes provide the basis for the gradient techniques. These modes also imprint their structure on the slow modes, while the fast modes provide a subdominat contribution. Thus we focus on Alfvénic turbulence below.

We assume that the injection of turbulent energy takes place at the scale  $L_{\rm inj}$ . If the injection velocity  $V_L$  equals the Alfvén velocity  $V_A$ , the Alfvénic turbulence naturally produces the Kolmogorov scaling in the direction perpendicular to the magnetic field. Indeed, as we mentioned earlier, motions induced by Alfvénic turbulence are not constrained by the magnetic field, and therefore they produce an energy cascade  $v_l^2$ , where l is the eddy size perpendicular to the magnetic field. The cascading to smaller scales that occurs over the eddy turnover time is  $\sim l/v_l$ . For l significantly larger than the dissipation scale, the flow of kinetic energy  $v_l^3/l$  is constant. In this way, we easily obtain the GS95 scaling for the motions perpendicular to the magnetic field, i.e.,  $v_l \sim l^{1/3}$ .

To determine how eddies evolve in the direction parallel to the magnetic field, we need to take into account that the mixing motions associated with magnetic eddies send out Alfvén waves with a period equal to the period of an eddy, i.e.,

$$l/v_l \approx l_{\parallel}/V_{\rm A},$$
 (1)

where  $l_{\parallel}$  is the parallel scale of the eddy. The condition (Equation (1)) is associated in the theory of GS95 with the critical balance, stressing the fact that Alfvén modes, which are by definition incompressible (see Biskamp 2003), have zero velocity divergence throughout the entire space. As a result, the infall velocity gradient  $v_l/l$  should be equivalent to that of the propagating velocity gradients  $V_A/l_{\parallel}$  of the Alfvénic wave along the magnetic field line. Combining this with the relation for  $v_l \sim l^{1/3}$ , we obtain the relation between the parallel and perpendicular scales of the eddies, i.e.,  $l_{\parallel} \sim l^{2/3}$ . This is the relation that is true for the eddies that are aligned with the local direction of the magnetic field that surrounds them. The velocities associated with a turbulent eddy are anisotropic, and thus the greatest change in velocity is in the direction perpendicular to the local direction of the magnetic field.

In both sub-Alfvénic and super-Alfvénic turbulence, the gradient methods of tracing the magnetic field can be used (see Yuen & Lazarian 2017b). However, the signatures of gradients in sub-Alfvénic and super-Alfvénic turbulence are different. For sub-Alfvénic turbulence, i.e., for  $V_L < V_A$ , the magnetic

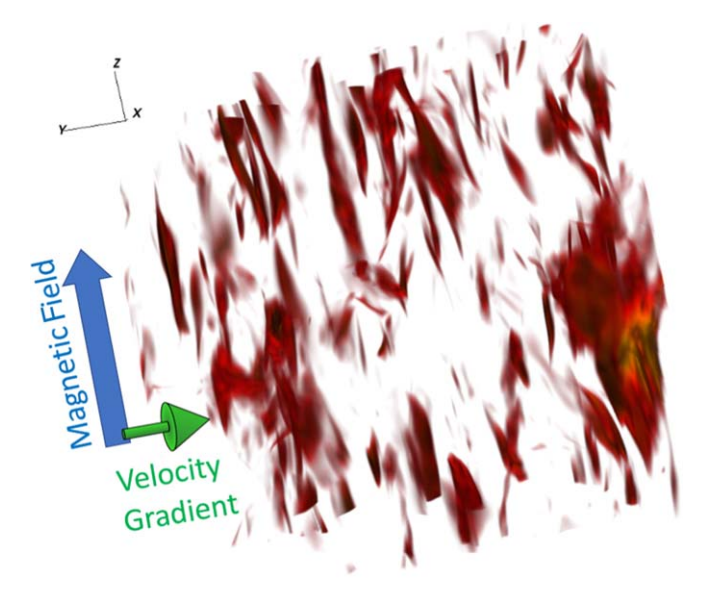


**Figure 1.** Isocontours of equal velocities for the sub-Alfvénic MHD turbulence simulation from our model Ma0.4 (see Table 1). It is clear that the gradients of the velocity structures are perpendicular to the magnetic field. From Lazarian & Yuen (2018a).

fields are always important and their action is imprinted on turbulent velocities at all scales. Figure 1 illustrates the alignment of the isocontours of equal velocity (red) and the mean magnetic field direction (blue) in numerical simulations with  $M_{\rm A}=0.4$  (see Chen et al. 2016; Hull et al. 2017). It is obvious from Figure 1 that the direction of the fastest spatial change in velocity is perpendicular to the magnetic field.

In the case of super-Alfvénic turbulence, extra complications in filtering large-scale isotropic eddies are encountered before the VGT method can be applied. The cases of energy injection with  $V_L < V_A$  and  $V_L > V_A$  are discussed in Appendix A. As we discuss there for the super-Alfvénic turbulence, i.e., for  $V_L > V_A$ , there is a range of scales for which turbulence is hydrodynamic and is not much affected by the magnetic fields. However, for a turbulence with an extended inertial range, there is a scale  $L_{\rm inj} M_A^{-3}$  at which the turbulent velocities become equal to the Alfvén velocity (see Lazarian 2006). Starting from that scale, our considerations above that relate the direction of the velocity gradients and of the local magnetic field are applicable.

In the case of super-Alfvénic turbulence scales larger than  $L_{\rm inj}M_{\rm A}^{-3}$ , turbulence eddies are isotropic (see Appendix A). As a result, one cannot derive velocity gradient information on these large-scale eddies, and therefore the gradient method cannot be used on isotropic large-scale eddies to trace magnetic fields. Turbulent eddies with scales smaller than  $L_{\rm inj}M_{\rm A}^{-3}$  are still anisotropic, and their gradients still probe the local direction of the magnetic field (see Yuen & Lazarian 2017b). As a result, in the case of super-Alfvénic turbulence, the velocity gradients at large scales are not sensitive to the magnetic field. However, this contribution can be spatially filtered out, as was demonstrated in LY17.

### 2.2. 3D Gradients Induced by MHD Turbulence

With this understanding of turbulence in hand, it is easy to understand how the VGT works. It is clear from Equation (8) that the anisotropy of eddies increases with the decrease in scale *l*. Thus the turbulent motions of eddies are increasingly

<sup>&</sup>lt;sup>10</sup> The closure relations employed in GS95 assume that the calculations were made in the reference frame of the mean field. Numerical simulations confirm that the GS95 relations are not correct in the mean field reference frame, but only correct in the local magnetic field reference frame.

better aligned with the local magnetic field as the eddy scale decreases. This property of eddies is the cornerstone of the VGT that we introduced in a series of recent papers.

In terms of practical measurements, it is easy to see that the gradients in turbulent flow increase with the decrease in scale. This increase can be estimated as  $v_l/l \sim l^{-2/3}$ , where Equation (9) is used. This suggests that the gradients arising from the smallest resolved eddies  $l_{\min}$  dominate the gradient measurements. When such eddies are well aligned with the direction of the magnetic field, the magnetic field at the  $l_{\min}$  scale can be traced by turning the velocity gradients by  $90^{\circ}$ .

### 2.3. Velocity Gradients Available through Observations

The 3D velocity fluctuations are not directly available from observations. Instead, we demonstrated that the gradients of velocity centroids (González-Casanova & Lazarian 2017; Yuen & Lazarian 2017a) and the gradients of intensity fluctuations measured within thin channel maps (Lazarian & Yuen 2018a) can be used as proxies of the velocity gradients. In both cases, the gradients are measured for a turbulent volume extended by  $\mathcal{L} > L_{\rm inj}$  along the LOS, and this entails additional complications, where  $\mathcal{L}$  is the LOS depth. While eddies stay aligned with respect to the local magnetic field, the direction of the local magnetic field is expected to change along the LOS. Thus the contributions of velocity gradients are summed along the LOS.

It is possible to show (see Lazarian & Pogosyan 2012) that for  $\mathcal{L} > L_{\rm inj}$ , the local system of reference <sup>12</sup> is not available from observations. Thus the reference system related to the mean magnetic field needs to be used. In this system of reference, the anisotropy of the eddies is determined by the anisotropy of the largest eddies, as illustrated in Figure 2. Indeed, the smallest eddies are aligned with the magnetic field, and this magnetic field varies along the LOS due to the large-scale variations of the magnetic field arising from the largest eddies (see Cho et al. 2002b). The latter variations are determined by the fluctuations of the magnetic field variations at the injection scale, i.e., the changes in the direction of the magnetic field along the LOS are  $\delta \varphi \approx \delta B/B \approx M_{\rm A}$ . We would like to stress that the tensors describing the fluctuations in the local and the global system of reference are different (e.g., compare the tensors in Cho et al. 2002b and Lazarian & Pogosyan 2012).

We have shown earlier that the 3D gradients of the value of 3D velocities are dominated by the smallest scales. A similar conclusion can be obtained for 2D observables. Indeed, the spectrum of observed fluctuations changes due to the LOS averaging. It is easy to show that the 2D spectrum of turbulence obtained by projecting the fluctuations from 3D has the same spectral index of -11/3 (see Lazarian & Pogosyan 2000). The relation between the spectral slope of the correlation function and the slope of the turbulence power spectrum in 2D in this situation is -11/3+2=-5/3, where 2 is the dimensionality of the

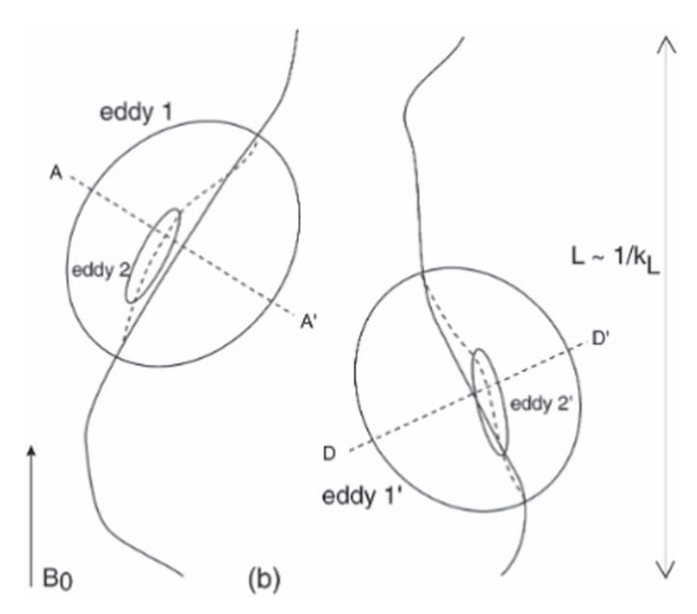


**Figure 2.** Illustration of the structure of anisotropic eddies. The small eddy 2 is aligned to the magnetic field of the larger eddy 1. The same is true for eddy 1', which is aligned to the magnetic field of eddy 2'. However, if measurements of eddies 2 and 2' are made with respect to the mean magnetic field  $B_0$ , both eddies 2 and 2' are treated as "misaligned" and contribute anonymously to the statistical tools (e.g., correlation function) with additional perpendicular-to-field contributions. From Cho et al. (2002b).

space. Therefore, the 2D velocity fluctuations arise from the 3D Kolmogorov-type turbulence scale as  $l_{\rm 2D}^{5/6}$ , with the gradient anisotropy scaling as  $l_{\rm 2D}^{-1/6}$ . This means that the contribution of the smallest scales is dominant for the measured 2D gradients.

### 2.4. MHD Turbulence Anisotropies and Distributions of the Gradient Orientations

Alfvénic turbulence is anisotropic, with its anisotropy given by the relations that we have described above. The anisotropy of Alfvénic turbulence imprints the scaling of the Alfvén modes into the anisotropy of slow modes (GS95, Lithwick & Goldreich 2001; Cho & Lazarian 2002). Alfvén and slow modes together carry most of the energy of the turbulent cascade. Fast modes, in many cases, are subdominant in terms of the energy cascade, although they play a very important role for a number of key astrophysical processes, e.g., cosmic ray scattering (see Yan & Lazarian 2002, 2004; Brunetti & Lazarian 2007). The fast modes stay "isotropic" for the pressure-dominated (i.e.,  $\beta = 2M_A^2/M_s^2 > 1$ , GS95) as well as for the magnetically dominated case (i.e.,  $\beta < 1$ ; Cho & Lazarian 2002). In what follows, we focus on the Alfvénic anisotropies that are measured in the observer's frame (see LP12).

It is important to keep the statistical nature of turbulence in mind. The velocity fluctuations have a distribution of directions about the magnetic field direction. Thus the velocity gradients also have a distribution of directions, the peak of which is perpendicular to the magnetic field direction. The properties of the distribution are, however, very informative. It follows from the theory of Alfvénic turbulence that the dispersion of turbulence wave vector directions changes with the Alfvén Mach number  $M_{\rm A}$ 

 $<sup>\</sup>overline{11}$  This effect is similar to that of summing far-infrared polarization from aligned grains along the LOS (see Andersson et al. 2015), with the exception that the polarization sums quadratically (e.g.,  $Q \propto \int dz b_y^2 - b_x^2$ ) in the form of Stokes parameters, while gradients are summed as linear vectors (e.g.,  $\nabla C \propto \int dz \nabla (\rho v)$ ). The difference between the two ways of summation is small for small  $M_A$ , but it becomes significant for large  $M_A$ . In the case of super-Alfvenic turbulence, the averaged magnetic field is better represented by the linear summation of gradients than the quadratic summation of dust polarization along the line of sight.

<sup>&</sup>lt;sup>12</sup> It is important to refer to the local system of reference because the direction of the local magnetic field defines the direction of the eddy anisotropy in magnetized turbulent media (LV99; Cho & Vishniac 2000; Maron & Goldreich 2001; Cho et al. 2002a).

<sup>&</sup>lt;sup>13</sup> We put isotropic in quotation marks, as the tensor describing fast modes is different from the tensor of isotropic turbulence (see more explanations in Lazarian & Pogosyan 2012).

(see Lazarian & Pogosyan 2016). This should be reflected in the distribution of the directions of gradients, and the goal of this paper is to determine this relation.

We consider first the sub-Alfvénic and trans-Alfvénic turbulence. This degree of anisotropy is characterized by the ratio of the maximum to minimum value of the correlation function because the relative orientation between the correlation direction and the magnetic fields changes from parallel to perpendicular. Evidently, for Alfvén and slow modes, the correlation will be maximum along the direction of the magnetic field. Clearly, there exists a correlation between the correlation function anisotropies and the gradients (Yuen et al. 2018b). We also address the correlation in Section 4.

From the discussion above, it is evident that the maximum of the velocity gradients is perpendicular to the longest axis of the eddies. This is true both for the 3D eddies and their LOS projections. Within the procedure of block averaging (Yuen & Lazarian 2017a), the distribution of the gradient orientation is fit with a Gaussian function, where the peak of the Gaussian is associated with the direction of the velocity gradients within the block.

The Gaussian function used in Yuen & Lazarian (2017a) is a three-parameter function:  $A \exp(-\alpha(\theta - \theta_0)^2)$ . Whether the other two fitting parameters are correlated to the intrinsic physical condition of MHD turbulence is unknown. However, it can be understood very easily that the height of the fitting function A and the width  $1/\sqrt{\alpha}$  are both related to the turbulence magnetization given by the Alfvén Mach number  $M_A$ . Indeed, if the turbulent injection velocity  $V_L$  is significantly slow compared to the Alfvén velocity, i.e.,  $M_A$  is small, then the bending of magnetic field is limited. The Alfvénic turbulence at small scales takes place through eddies that mix magnetic field lines perpendicular to the local magnetic field direction. For small  $M_A$ , all magnetic field lines are approximately in the same direction, and therefore the dispersion of the velocity gradients that are perpendicular to magnetic field lines is small. As the turbulence driving increases in amplitude, the dispersion of the velocity gradient orientations is expected to increase. In the framework of the distribution of the gradient orientations, a more prominent peak (i.e., higher A and large  $\alpha$ ) is expected for small  $M_A$ . Therefore one can infer the magnetization of a turbulent region by analyzing the amplitudes of A and  $\alpha$ .

The magnetization can also be studied in the case of super-Alfvénic turbulence. As we discuss in Appendix A, for scales larger than the scale at which the turbulent velocity is equal to  $V_A$ , the correlation between the magnetic field direction and the direction of the velocity fluctuations decreases. However, we here study moderately super-Alfvénic turbulence, and therefore the this correlation does not disappear completely. This allows us to obtain  $M_A$  from the distribution function of the gradients. The latter is another name for the distribution of the gradient orientations that we will use further.

Figure 3 illustrates the distribution of the gradient orientations for sub-Alfvénic, trans-Alfvénic, and super-Alfvénic turbulence. The block-averaging procedure (Yuen & Lazarian 2017a) is used. The block size is chosen sufficiently large to allow Gaussian fitting. The latter is the necessary for the gradient technique that we have developed. A good Gaussian fit is important to assess how reliable the magnetic field direction is that we obtain with our technique, and also for

determining the magnetization, as we discuss in this paper. We clearly see that the width of the distribution increases with the increase of  $M_{\rm A}$ . Similarly, the amplitude of the Gaussian distribution given by the ratio of the top-base values (see Figure 3) decreases with  $M_{\rm A}$ . We discuss the quantitative measures that can translate the parameters of the distribution of the gradient orientations into the  $M_{\rm A}$  data.

#### 2.5. Magnetic Field and Density Fluctuations

It is necessary to mention that our earlier studies have shown that the magnetic field direction can be traced with magnetic gradients that are available, e.g., using synchrotron emission. The considerations about velocity symmetry and magnetic fluctuations within Alfvénic turbulence constitute the basis for tracing the magnetic field using not only the VGT, but also the synchrotron intensity gradients (SIGs) Lazarian et al. (2017) and the SPGs (Lazarian & Yuen 2018b).

All our considerations above relevant to the distribution functions of velocity gradients are applicable to the SIGs and the SPGs. Therefore we expect to obtain  $M_{\rm A}$  through studying the distribution of the gradient orientations of the synchrotron intensities and the synchrotron polarization. We defer presenting the corresponding results to other publications.

Unlike the velocity and magnetic field fluctuations, the density fluctuations are not a direct tracer of MHD turbulence. At small sonic Mach number  $M_s$ , the densities act as a passive scalar and follow the general pattern of the velocity fluctuations (Cho & Lazarian 2003; Kowal et al. 2007). The proxies available from observations are the IGs. If they are calculated using our recipes of block averaging for small  $M_s$ , they can also trace magnetic fields. At the same time, being sensitive to shocks, the IGs can be successfully combined with the velocity or magnetic gradient measures, i.e., the velocity centroid gradients (VCGs; González-Casanova & Lazarian 2017; Yuen & Lazarian 2017a), VChGs (Lazarian & Yuen 2018a), SIGs (Lazarian et al. 2017), or SPGs (Lazarian & Yuen 2018b), for tracing both magnetic fields and shocks (see YL17b).

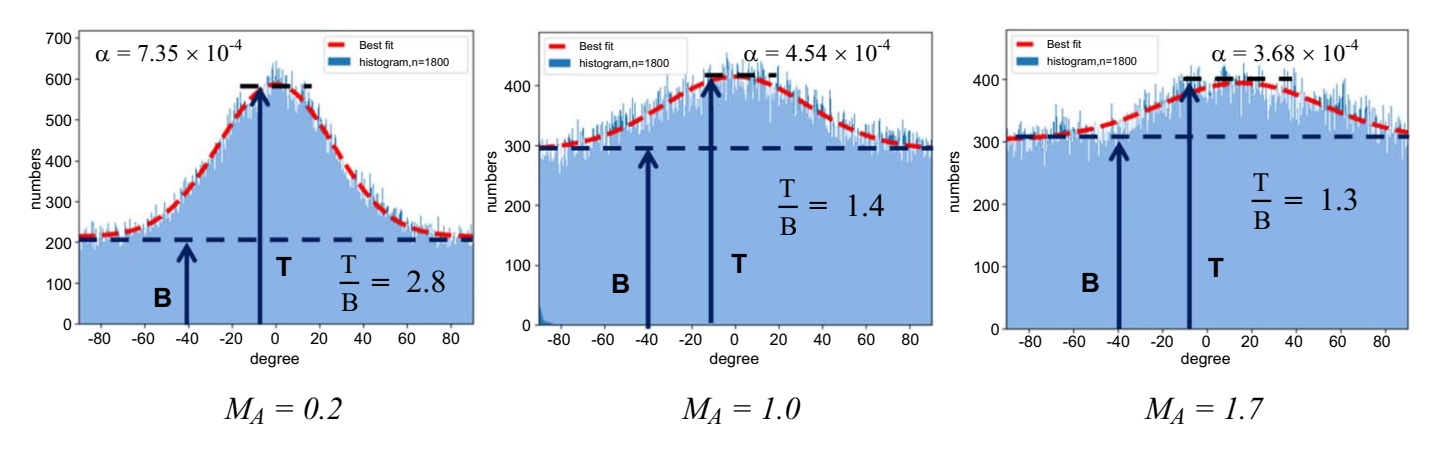
As densities are sensitive to shocks, we expect to observe that the distribution functions of IGs are both functions of  $M_s$  and  $M_A$ , the dependence on the former being dominant for high  $M_s$ . We do not discuss the properties of the distribution functions of IGs in this paper.

### 3. Numerical Approach

We use 10 numerical cubes for the current study. Table 1 presents the list of the MHD compressible simulations, some of which have been used in Yuen & Lazarian (2017b) and Lazarian & Yuen (2018a). The latter paper provides the details of the 3D MHD simulations we employed.

For our set of simulations, the sonic Mach number is kept approximately constant ( $M_s \sim 5.5$ –7.3) since we are more interested in studying the effect of the Alfvénic Mach number  $M_A$  on the distribution functions of gradient orientations. The chosen  $M_s$  are within the range of sonic Mach numbers relevant to molecular clouds (Zuckerman & Palmer 1974). Observationally, one can approximate  $M_s$  by either studying the amplitudes of the velocity gradients (see Yuen et al. 2018b) or investigating the width of the density probability distribution function (Burkhart & Lazarian 2012).

### **Angle Dispersion**



### Angle Dispersion (Channel)

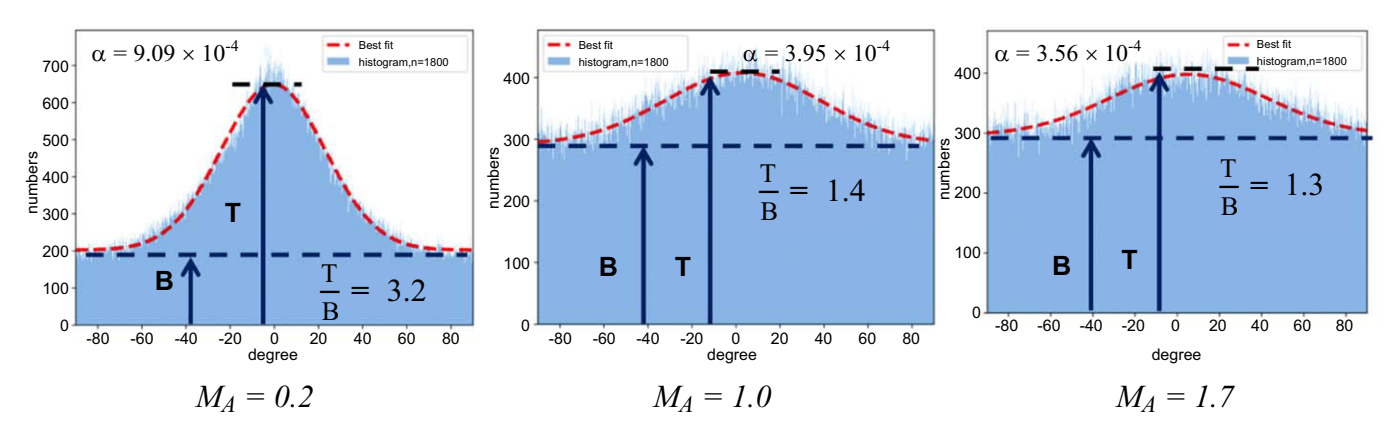


Figure 3. Upper panel: the three panels show the velocity centroid gradient orientation histograms from three numerical cubes with different Alfvénic Mach number  $M_A$ . We fit the three Gaussians with a modified Gaussian profile. T and T mean the peak and bottom value of the modified Gaussian profile, which is defined as T = A + C' and T and T are T and T are T are T and T are T are T and T are T and T are T are T are T and T are T are T are T and T are T and T are T are T and T are T and T are T and T are T and T are T are T are T and T are T are T and T are T and T are T are T and T are T are T are T are T are T and T are T are T are T and T are T and T are T and T are T are T and T are T are T and T are T and T are T are T and T are T are T and T are T and T are T are T and T are T are T and T are T and T are T and T are T and T are T are T and T are T are T and T are T are T are T and T are T and T are T are T are T are T are T and T are T and T are T are T are T and T are T are T a

Figure 1 provides a visualization of velocity structures in one of our cubes. As we mentioned earlier, the isocontours of equal velocity are aligned with the magnetic field, which causes the velocity gradients to be directed perpendicular to magnetic field.

As we discussed earlier, the point-wise velocity information is not directly available. In this situation we calculate either velocity centroids or intensities within thin channel maps. Below we discuss both measures.

Velocity centroids. The normalized velocity centroid  $Ce(\mathbf{R})$  in the simplest case <sup>14</sup> and the emission intensity  $I(\mathbf{R})$  are defined as

$$Ce(\mathbf{R}) = I^{-1} \int \rho_{\nu}(\mathbf{R}, \nu) \nu d\nu,$$

$$I(\mathbf{R}) = \int \rho_{\nu}(\mathbf{R}, \nu) d\nu,$$
(2)

where  $\rho_{\nu}$  is density of the emitters in position–position–velocity space,  $\nu$  is the velocity component along the LOS, and R is the

 Table 1

 Description of Our MHD Simulations

		1		
Model	$M_S$	$M_{\mathrm{A}}$	$\beta = 2M_{\rm A}^2/M_{\rm S}^2$	Resolution
Ma0.2	7.31	0.22	0.01	792 <sup>3</sup>
Ma0.4	6.1	0.42	0.01	$792^{3}$
Ma0.6	6.47	0.61	0.02	$792^{3}$
Ma0.8	6.14	0.82	0.04	$792^{3}$
Ma1.0	6.03	1.01	0.06	$792^{3}$
Ma1.1	6.08	1.19	0.08	$792^{3}$
Ma1.4	6.24	1.38	0.1	$792^{3}$
Ma1.5	5.94	1.55	0.14	$792^{3}$
Ma1.6	5.8	1.67	0.17	$792^{3}$
Ma1.7	5.55	1.71	0.19	792 <sup>3</sup>

**Note.**  $M_s$  and  $M_A$  are the instantaneous values at each of the snapshots are taken. This refers to set C in the lower panel of Figure 5.

2D vector in the pictorial plane. The integration is assumed to be over the entire range of v. Ce( $\mathbf{R}$ ) is also an integral of the velocity and LOS density, which follows from a simple transformation of variables (see Lazarian & Esquivel 2003). For a constant density, this is the velocity averaged over the LOS.

<sup>&</sup>lt;sup>14</sup> Higher-order centroids are considered in Yuen & Lazarian (2017b), and they have  $v^n$ , e.g., with n=2, in the expression of the centroid. Such centroids may have additional advantages because they are more focused on studying velocity fluctuations. However, for the sake of simplicity, we employ for the rest of the paper n=1.

Fluctuations within channel maps. Another measure that we employ is the channel map intensity. This is the emission intensity integrated over a range of velocities, i.e.,

$$I_{\delta \nu}(\mathbf{R}) = \int_{\delta \nu} \rho_{\nu}(\mathbf{R}, \nu) d\nu, \tag{3}$$

where  $\delta v$  is the range of velocities for the integration.

The thin channel condition. If  $\delta v$  is smaller than the velocity dispersion for the eddies under study, for such eddies the velocity slices were termed "thin" in Lazarian & Pogosyan (2000, henceforth LP00; see also Lazarian & Yuen 2018a). For such slices the intensity fluctuations arising from the eddies are mostly induced by the velocity fluctuations (LP00).

#### 4. Results

### 4.1. Determining $M_A$ with the Distribution of the Gradient Orientations

We investigate how the change in  $M_A$  would alter the behavior of the distribution of the gradient orientations. Distribution functions of the gradients for both centroids Ce  $(\mathbf{R})$  and velocity channel intensities  $I_{\delta V}$   $(\mathbf{R})$  are presented in Figure 3. These distribution functions are constructed by histograms with 1800 bins from three sets of numerical cubes with different  $M_A$ . We fit the gradient orientation histogram using the Gaussian profile proposed in YL17a by adding one constant shifting term, i.e.,

$$F = A \exp(-\alpha(\theta - \theta_0)^2) + C'. \tag{4}$$

The value of the shift<sup>15</sup> C' and of coefficient A change with  $M_A$ , which provides a way to study the Alfvén Mach number using the top-base ratio (C'+A)/C'. The fitting lines for each panel are shown as red dashed lines in Figure 3. The width of the Gaussian profile increases with respect to  $M_A$ , while the top-base ratio decreases with the increase in  $M_A$ . The calculations were performed using block averaging (see Yuen & Lazarian 2017a) and choosing blocks large enough to ensure that the Gaussian fitting is sufficiently accurate. By performing similar calculations for different simulations from Table 1, we observe noticeable changes in the distribution of gradients.

The standard deviation of the gradient orientation  $\sigma_{\rm GD}$  can be characterized by circular statistics,

$$\sigma_{\text{GD}} = \sqrt{\log \frac{1}{R^2}}$$

$$= \sqrt{-\log(\langle \cos \theta \rangle^2 + \langle \sin \theta \rangle^2)},$$
(5)

where  $\theta$  is the gradient orientation of each pixel. Note that in the formula, the range of  $\theta \in [-\pi, \pi]$ ; but the observational gradient orientation in observational data (denoted as  $\tilde{\theta}$ ) is in the range  $[-\pi/2, \pi/2]$ . In order to calculate the inverted

 Table 2

 Extra Simulation Used for Producing the Lower Right Panel of Figure 5

Set	Model	$M_s$	$M_{ m A}$	Resolution
A	Ms0.2Ma0.02	0.2	0.02	480 <sup>3</sup>
	Ms0.2Ma0.07	0.2	0.07	$480^{3}$
	Ms0.2Ma0.2	0.2	0.2	$480^{3}$
	Ms0.20Ma0.66	0.20	0.66	$480^{3}$
	Ms0.2Ma2.0	0.2	2.0	$480^{3}$
	Ms0.20Ma0.66	0.20	0.66	$480^{3}$
	Ms0.02Ma0.2	0.02	0.2	$480^{3}$
В	Ms0.4Ma0.04	0.41	0.04	$480^{3}$
	Ms0.8Ma0.08	0.92	0.09	$480^{3}$
	Ms1.6Ma0.16	1.95	0.18	$480^{3}$
	Ms3.2Ma0.32	3.88	0.35	$480^{3}$
	Ms6.4Ma0.64	7.14	0.66	$480^{3}$
	Ms0.4Ma0.132	0.47	0.15	$480^{3}$
	Ms0.8Ma0.264	0.98	0.32	$480^{3}$
	Ms1.6Ma0.528	1.92	0.59	$480^{3}$
	Ms0.4Ma0.4	0.48	0.48	$480^{3}$
	Ms0.8Ma0.8	0.93	0.94	$480^{3}$
	Ms0.132Ma0.4	0.16	0.49	$480^{3}$
	Ms0.264Ma0.8	0.34	1.11	$480^{3}$
	Ms0.04Ma0.4	0.05	0.52	$480^{3}$
	Ms0.08Ma0.8	0.10	1.08	$480^{3}$
D	d0	5.0	10.0	$480^{3}$
	d1	0.1	10.0	$480^3$ , $640^3$ , $1200^3$
Е	e1	0.5	5.0	$480^{3}$

**Note.** Set C in Figure 5 is exactly what we showed in Table 1.

variance  $R = \sqrt{\langle \cos \theta \rangle^2 + \langle \sin \theta \rangle^2}$ , we perform  $\theta = 2\tilde{\theta}$  when processing the observational data. The quantity 1 - R is called the variance in circular statistics, which provides an alternative measure of the dispersion for a set of directional data, and we use this parameter in the following sections.

We also evaluate the top-base ratio by dividing the peak value of the Gaussian peak from the base value in the gradient orientation histogram (see Figure 3). We expect that both of them are related to the Alfvénic Mach number  $M_A$  as we explained in Section 2. Figure 3 illustrates how the fitting parameters for the distribution and the top-base ratio are obtained. Apparently, for low  $M_A$ , the distribution is strongly peaked and A is large. This corresponds to a good alignment of individual gradient vectors and the magnetic field direction. As  $M_A$  increases, the gradient distribution is aligned with the magnetic field only in the statistical sense. This is especially obvious for  $M_A > 1$  as the velocity motions at large scales become uncorrelated with the magnetic field.

The panels in Figure 4 compare the dependences of the variances and top-base ratios obtained for the centroid and channel gradients. We observe that both these measures decrease as  $M_A$  increases, which suggests that the top-to-base ratio and inverted variance are sensitive measures of  $M_A$  in the range of [0.2, 1.7].

In general, the findings for the gradients in Figures 3 and 4 are easy to understand. They can be explained by a simple physical argument: When the magnetization is stronger (i.e.,  $M_A$  smaller), gradients tend to be more aligned with each other, therefore the peak of the histogram is more prominent (higher top-base ratio) and narrow (lower  $\sigma_{GD}$ ).

To extract the power-law dependency of 1 - R to  $M_A$ , we plot the relation of (1 - R) versus  $M_A$  (see upper right panel of Figure 5). While there is a well-fit power law of

 $<sup>\</sup>overline{^{15}}$  In principle, the Gaussian profile with a shifting term is a better representation of the gradient orientation distribution in numerical simulations, since the histogram bin away from the peak of the gradient orientation distribution is usually much higher than zero. For instance, with  $M_{\rm A} \sim 0.2$ , the velocity isocontour axis ratio can be in the hundreds (Xu & Lazarian 2018). However, current simulations have limited resolutions. There is a natural tendency for the velocity contours to have a lower axis ratio because the minor axis cannot be resolved. As a result, the histogram bin away from the peak of the gradient orientation distribution would not be close to zero. A constant shift would address the issue of finite length. In practice, the shift will not change the prediction of the peak location by block averaging.

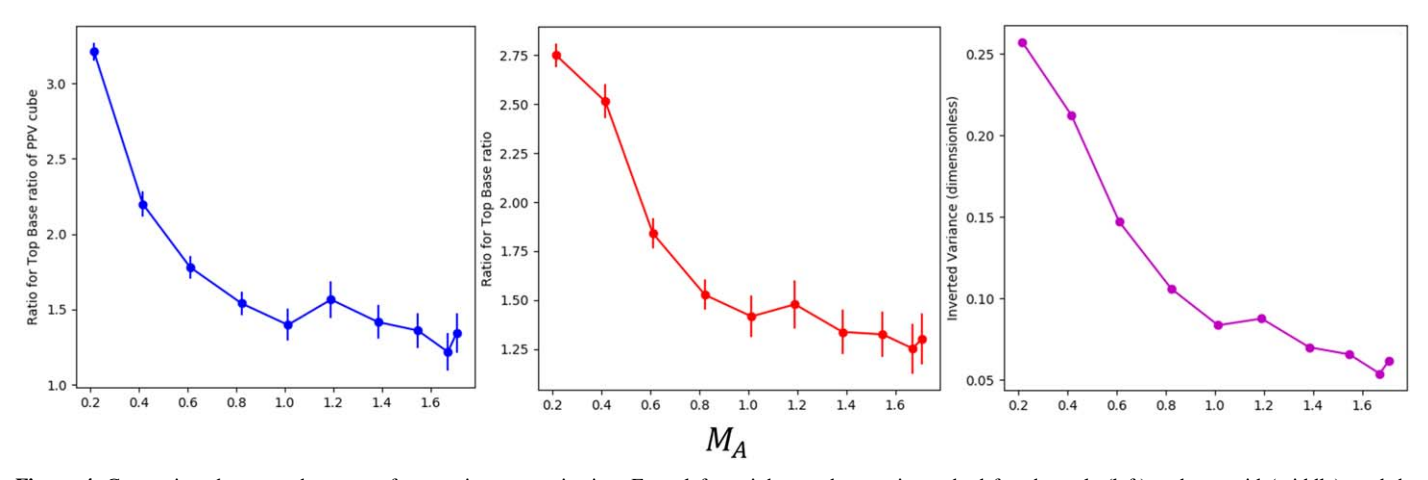


Figure 4. Comparison between the ways of measuring magnetization. From left to right: top-base ratio method for channels (left) and centroid (middle), and the inverted variance R method for the centroid (right). The three quantities are plotted against  $M_A$ . There is a similar decreasing trend for the three methods, especially for  $M_A < 1$ .

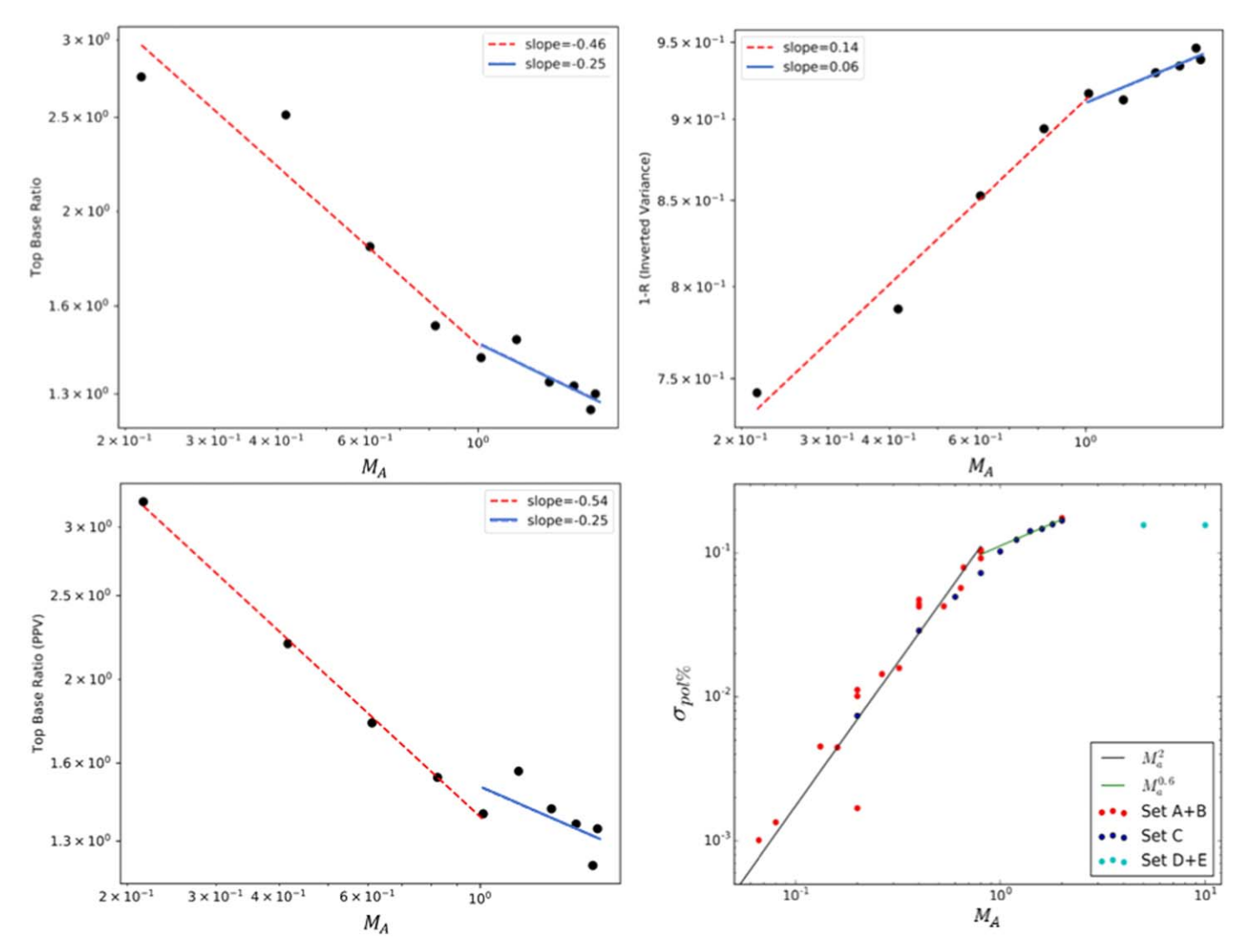


Figure 5. (Top left) The top-base ratio plotted against  $M_A$  in log-log space using the simulation set from Table 1. (Top right) Log-log plot using the simulation set from Table 1 showing the variation of 1 - R to  $M_A$ . We fit the scatter plot with two segments, bending at  $M_A \sim 1$ . (Lower left) Similar to the top left corner, but the data points from Table 1 computed from velocity channels instead of velocity centroids. (Lower right) The change of the polarization degree dispersion vs.  $M_A$  using the simulation set from Table 2.

 $(1-R) \propto M_{\rm A}^{0.14\pm0.03}$ , the fit is significantly flattened when  $M_{\rm A} \geqslant 1$ . Similarly, the top-base ratio also showed a two-segment behavior in Figure 5. The fit of the top-base ratio to  $M_{\rm A} < 1$  shows a power-law ratio of  $\propto M_{\rm A}^{-0.46\pm0.18}$ . The change in power law index for  $M_{\rm A} > 1$  is expected, as we have discussed earlier (see Appendix A), the nature of turbulence changes when the injection velocity becomes higher than the Alfvén speed. In this situation the large-scale motions are dominated by hydro-type turbulence, and the directions of the magnetic field within the flow are significantly randomized. This changes the distribution function of the gradient orientations.

### 4.2. Comparison with the Polarization Percentage Technique

To illustrate the power of the techniques we showed in Section 4.1, we would like to compare the results in Section 4.1 to methods applicable to polarimetry. In Appendix C we provide a new way of evaluating  $M_A$  using the dispersion of the polarization percentage  $\sigma_{\text{pol}\%}$ . While the traditional Chandrasekhar-Fermi technique uses the variations of polarization directions to determine  $M_A$ , the dispersion of the polarization percentage does not require knowledge of circular statistics. In Appendix C we show that the analytical expectation that  $\sigma_{\text{pol}\%} \sim M_{\text{A}}^2$  when  $M_{\text{A}} < 1$ , which agrees well with our numerical calculations shown in the lower right of Figure 5 from Table 2 obtained from 30 sets of independent numerical simulations. For  $M_A > 1$ , the dependence also changes due to the same reasons as we discussed in Section 4.1. For instance, the flattered fitting line with  $M_A \in [1, 2]$  has a proportionality of  $\sigma_{\rm pol\%} \propto M_{\rm A}^{0.6}$ . In comparison, for the gradient dispersion, the power law is  $(1 - R) \propto M_A^{0.06}$ .

## 4.3. Comparison with Other Techniques for Obtaining Magnetization

A number of other techniques for studying magnetization have been suggested. For instance, the Tsallis statistics (see Esquivel & Lazarian 2010) was shown to be sensitive to the value of  $M_{\rm A}$ . In addition, one can estimate for sub-Alfvénic turbulence that  $M_{\rm A}\sim\delta\phi$ , where  $\phi$  is the dispersion of the magnetic field directions. These directions can be obtained either through polarimetry studies, e.g., dust polarimetry, or using the variation in the velocity or in the magnetic field gradient orientations. <sup>16</sup>

Obtaining  $M_A$  through the Gaussian profile fitting requires that the conditions for the sub-block averaging in Yuen & Lazarian (2017a) are satisfied. In other words, the distribution of the gradient orientation has to be well fit by a Gaussian. Therefore the consistency of both directions (as traced by Yuen & Lazarian 2017a) and magnetization from this work are doubled-checked through the sub-block averaging algorithm, i.e., whenever the Gaussian profile is not properly fit, there should not be any probe by VGT on neither magnetic field directions nor magnetizations. While the velocity gradients present an independent technique for magnetic field tracing, it is synergetic with polarimetry measurements while dealing with the complex structure of interstellar magnetic fields.

A more elaborate tool for studying  $M_A$  is the analysis of the correlation function anisotropy (CFA). This technique has been

explored in a number of publications (Esquivel & Lazarian 2011; Burkhart & Lazarian 2012; Burkhart et al. 2014; Esquivel et al. 2015; Kandel et al. 2016, 2017a), and we illustrate its results in Appendix B.

The advantage of the CFA technique is the existence of the analytical description that relates the measurements not only to  $M_{\rm A}$ , but to the properties of the fundamental MHD modes, i.e., Alfvén, slow, and fast modes (Lazarian & Pogosyan 2012; Kandel et al. 2016, 2017a, 2017b) However, the CFA technique requires calculating correlation functions and therefore is less local than the technique in this paper. Further research should reveal the synergy between different techniques of determining  $M_{\rm A}$ .

### 4.4. Effects of Adding Noise

In this section we show that the new technique of finding  $M_A$  works in the presence of noise. We add white noise with amplitudes relative to the standard deviation of the velocity centroid  $\sigma_C$  and test how the power law is changed as a function of noise amplitudes. In our test we apply white noise with amplitudes  $0.1\sigma_C$  and  $0.2\sigma_C$  and compare our results with the original fit we showed in Figure 5. For noise suppression, we employ the Gaussian smoothing of  $\sigma=2$  pixel as proposed in Lazarian et al. (2017). According to Lazarian et al. (2017), the kernel size we picked here would preserve most of the small-scale structures while efficiently suppressing the noise in the synthetic map globally. By adding the noise and also the smoothing kernel, we can then test whether in noisy observations we can still use the top-base ratio and variance methods to estimate magnetization.

Figure 6 shows the log-log plot of both (1-R) versus  $M_A$  and the top-base ratio to  $M_A$  with noise addition (left) and smoothing (right). Before smoothing, the noise-added (1-R) versus  $M_A$  relation is very sensitive to the noise level, where only  $0.2\sigma_C$  can already flatten the plot. Fortunately, the application of the smoothing technique shows that the magnetization tracing is not changed significantly. This gives us confidence in applying our technique to observations.

### 4.5. Observational Data Analysis

We would like to demonstrate the application of the technique using GALFA-H I data. For details, we refer to the respective survey paper (Peek et al. 2018). The Galactic Arecibo L-band Feed Array H I (GALFA-H I) survey is a survey of the Galaxy in the 21 cm neutral hydrogen line. The data are obtained with the Arecibo Observatory 305 m telescope. The telescope angular resolution is 4'. The region covers the sky at right ascension (R.A.) across 263°5–196°6, and declination (decl.) across 22°5–35°3. These data also cover a wide range of galactic latitudes from medium to high, which is 26°08–83°71. The same region has been used in Clark et al. (2015) for the rolling Hough transform analysis.

As we mentioned earlier, the choice of the block size is an important step for analyzing the data with gradients. If the block size is too small, the Gaussian fitting is poor, which means that the determination of gradients is not reliable (see YL17a). If the block size is too large, the map is excessively coarse. Moreover, at large scales the regular variations of the direction of the Galactic magnetic field become important. As a result, the dispersion of angles increases with block size. These considerations in Lazarian & Yuen (2018a) were used to

<sup>&</sup>lt;sup>16</sup> Variations of the SIGs and SPGs can also be used. The advantage of the gradient techniques is that they are independent of Faraday rotation.

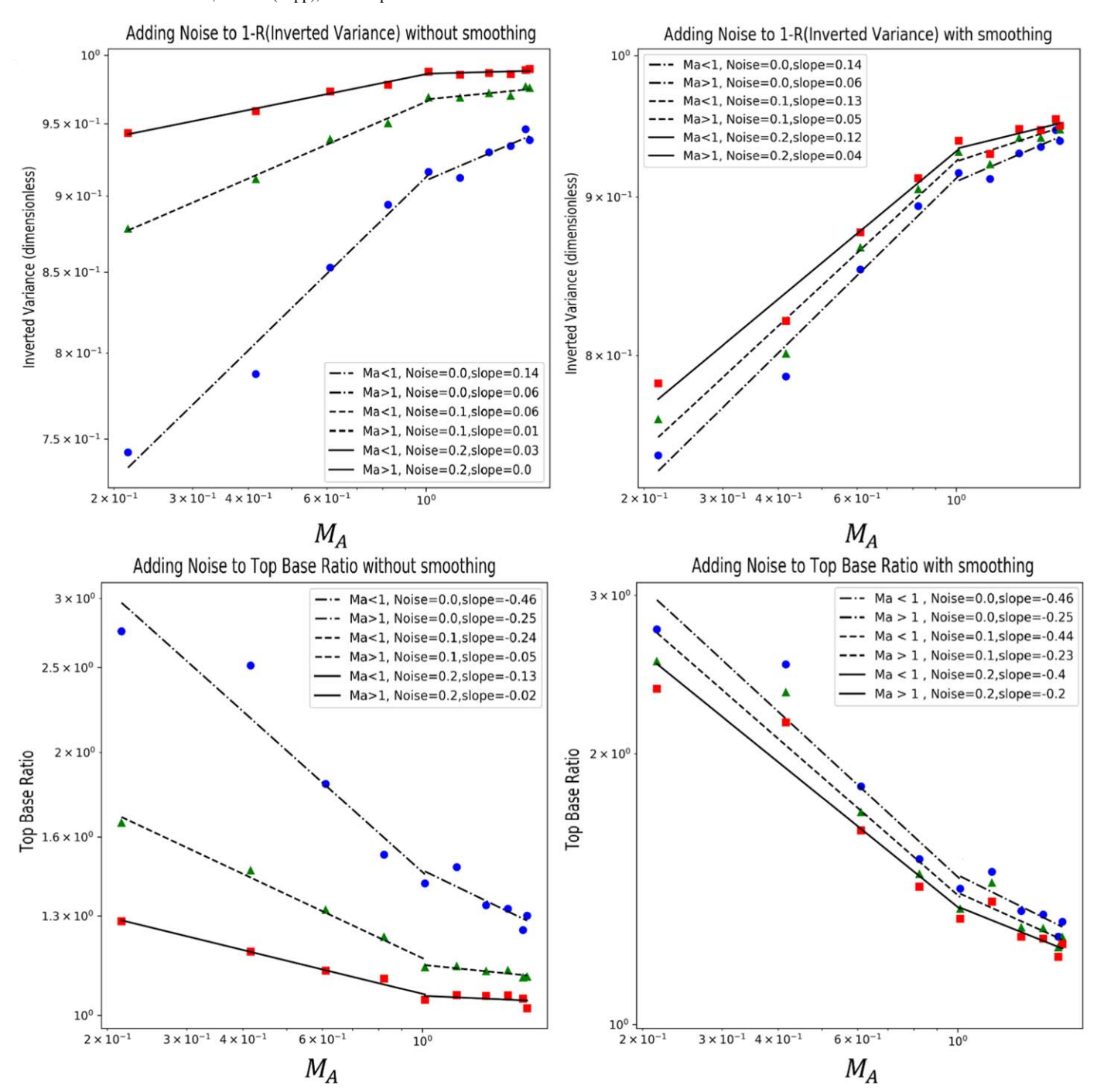


**Figure 6.** Four panels showing how noise and the suppression of it influences the result of the magnetization tracing. For the methods of dispersion (top row) and top-base ratios (bottom row), we add white noise (left column) to the map and see how the statistical parameters are altered. When the noise-suppression techniques for gradients (Lazarian et al. 2017) are used, the trend of the magnetization tracing (right column) is obviously more robust for both methods.

optimize the block size<sup>17</sup> for the GALFA-H I map that we also use in this paper.

We decompose the GALFA-H I map into blocks of size  $150^2$  pixels, in which one pixel is 4', and compute both the dispersion and top-base ratio of each block after a smoothing

Gaussian filter of 4 pixels. Figure 7 shows the result of the  $M_A$  distribution that we obtained with analyzing the distributions of the gradient orientations. We clearly see a similarity of the  $M_A$  map obtained using the top-base method and that obtained with the dispersion (in terms of the variance 1 - R) method. The fact that the two techniques provide very similar output increases our confidence in the distribution of  $M_A$  that we obtain.

In the top-base method, we marked the pixels as white (NaN), indicating that due to noise, the gradient angle distribution could not be reliably fit with a Gaussian profile.

<sup>17</sup> More sophisticated procedures have also been tested. For instance, one can filter out gradients with the largest and smallest amplitudes. The former corresponds to gradients arising from shocks (YL17b), the latter corresponds to noise. Fitting Gaussians into the remaining data can improve the data quality. We plan to explore this and other ways of improving the gradient studies elsewhere. In this paper we use the block averaging as presented in YL17a.

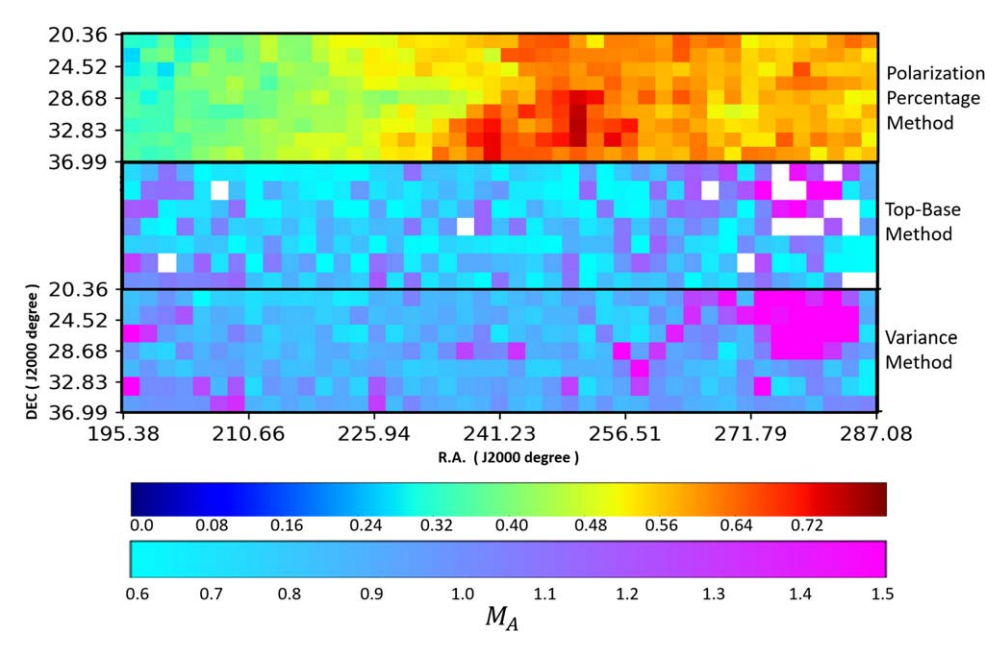


Figure 7. Top panel: prediction of  $M_A$  from the  $P_{\%}$  method. As a matter of fact (e.g., Lazarian 2007), the dust grain alignment drops significantly in low-latitude region (approximately on the right-hand side), which explains why the expected  $M_A$  in higher latitude will be significantly higher. A similar effect on the polarization percentage is also observed in Planck Collaboration et al. (2015). Middle panel:  $M_A$  distribution obtained using the top-base ratio approach from this paper on the region of GALFA-H I with a block size of  $150^2$  pixels. The data are taken from Clark et al. (2015) and Peek et al. (2018). The white pixels are the regions that cannot be fit with the Gaussian profile. Bottom panel: distribution of  $M_A$  obtained using the variance method. There is a similarity of the  $M_A$  predictions between the top-base ratio and the variance method.

For such points, the statistical variance was computed <sup>18</sup> using Equation (5). This study is the first of this kind and has illustrative purposes. The accuracy of this approach for the regions where the Gaussian fitting does not work well will be studied elsewhere. For consistency with the Gaussian fitting requirement in Yuen & Lazarian (2017a), we do not include the NaN data in the top-base method in the histogram in Figure 8.

We also test how the selection of the block size changes our estimate of  $M_A$ . Figure 8 shows the normalized distributions of  $M_{\rm A}$  of the piece of GALFA region (Figure 7) when we vary the block size for which we calculate the top-base ratio. While there is a fluctuation of the magnetization estimation for different block sizes, both the peak value and the shape of the distributions are very similar. One can observe that the peak values of these distributions are all around  $M_A \sim 0.75$ , and they exhibit a rough Gaussian profile. This suggests that the block size does not significantly change the estimate of  $M_A$ . However, we expect that the regular curvature of the magnetic field lines within the block, which induced a broadened distribution of the gradient orientation, is a factor that makes estimating  $M_A$  in high latitude H I difficult (see also the lower  $M_{\rm A}$  obtained with the same data with the gradient amplitude method in Yuen et al. 2018b). The issue of obtaining the accurate values of  $M_A$  in regions with regular curvatures definitely requires further detailed studies.

## 5. Obtaining the Magnetic Field Intensity Distribution from the $M_{\rm A}$ Distribution

The Alfvén Mach number  $M_{\rm A}$  is an essential characteristic of magnetized turbulent media that is important for describing key astrophysical processes, e.g., an explicit discussion of the dependence of cosmic ray propagation in Lazarian & Yan (2014) and Lazarian (2016) and heat conduction in Lazarian (2006).

In principle, if one can obtain accurate polarization measurements with a sufficiently high dust grain alignment efficiency (see Lazarian 2007), then the method of gradients has no particular advantage over polarization measurements. However, in observational environments, the polarization fraction is fairly low (e.g., in case of polarization measurements near molecular cloud centers), which will often lead to insufficient statistics in computing the dispersion of polarization angles. In contrast, the VGT is versatile in different physical regimes (Yuen & Lazarian 2017b; Lazarian & Yuen 2018a), and thus the estimation of magnetic field information (directions, and more importantly, magnetization) can be applied to a wider regime without any of the statistical problems we face in polarization measurements.

In addition, if the Alfvén Mach number is known, it is possible to obtain the magnetic field strength from the relation  $M_{\rm A}=\frac{\delta B}{B}$ . Assuming that the relation of  $\delta B$  and the dispersion of the velocity obeys the Alfvénic relation, i.e.,  $\delta V=\delta B/(4\pi\rho)^{1/2}$ , one can express the magnetic field strength as

$$B_{\rm POS} = \sqrt{4\pi\rho} \frac{\delta V}{M_{\rm A}},\tag{6}$$

where  $\delta V$  can be associated with the velocity dispersion, and we took into account that it is the plane-of-sky (POS) component of the magnetic field that is being explored with the technique. As only the LOS velocity  $\delta v_{\rm los}$  is available, for

<sup>&</sup>lt;sup>18</sup> In principle, even when the distribution of the gradient orientations does not follow Gaussian, we can still compute the statistical circular dispersions (and thus inverted variance) according to Equation (5). However, whether the values computed through Equation (5) have any meaning in the framework of VGT is yet to be investigated.

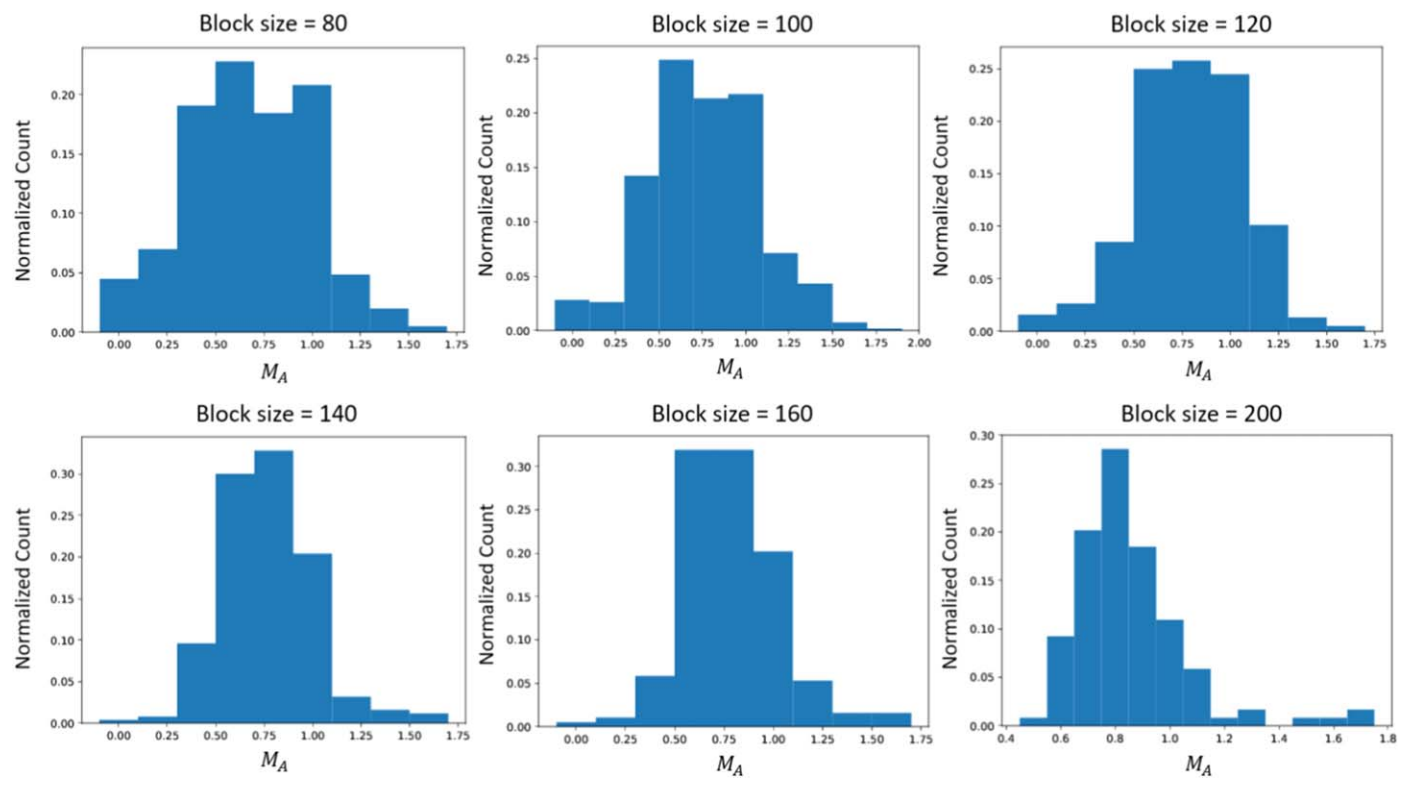


Figure 8. Estimated  $M_A$  for Figure 7 using the top-base ratio method in different block sizes. The peak  $(M_A \sim 0.75)$  remains unchanged, even through the sampling area increases by about  $2.5^2 \sim 6$  times.

the practical use of Equation (6), the velocity dispersion  $\delta V$  there should be associated with  $\delta v_{\rm los}$ , i.e.,  $\delta V = C \delta v_{\rm los}$ , where C is a coefficient that relates the dispersions of the turbulence POS velocities with those of the available LOS. For a uniformly distributed Alfvén wave that moves along the mean magnetic field line, C=0.5. The coefficient C increases when the angle between the mean magnetic field direction and the LOS is smaller. In the limiting case of a magnetic field parallel to the LOS, C is not defined, as no LOC velocities can be measured.

In reality, the observed magnetic field is not simply composed of a dominant mean field with straight-line morphology and infinitesimal Alfvén waves moving along the mean field. For realistic turbulence, the magnetic field wandering is significant (see LV99; Eyink et al. 2011). Moreover, MHD turbulence consists of three MHD cascade modes, namely the Alfvén, slow, and fast modes, in which every mode has unique cascade properties (see Lithwick & Goldreich 2001; Cho & Lazarian 2002). As a result, in most practical studies the coefficient *C* is treated as an empirically given parameter.<sup>19</sup>

In addition, the calculations are slightly more complicated for the case of small-scale turbulence injection (see Yoo & Cho 2014). We discuss the details of obtaining the magnetic field intensity from observations elsewhere. For the time being, it is important that Equation (6) provides a rough guidance for exploring the magnetic field strength.

#### 6. Discussion

### 6.1. Broader Applications to Other Types of Gradients

The cornerstone of this work is the Gaussian fitting function that was first used in Yuen & Lazarian (2017a). This provided us with ways of obtaining the dispersions and the top-based ratios that are used to trace  $M_A$ . While we obtained all the estimates of  $M_A$  for velocity centroids in this paper, we expect that the technique presented here is applicable to other measures, e.g., reduced centroid gradients from Lazarian & Yuen (2018a), SIGs from Lazarian et al. (2017), SPGs and synchrotron-derivative polarization gradients from Lazarian & Yuen (2018b), and IGs from Yuen & Lazarian (2017b). More importantly, we showed in Figure 3 that in the dispersion of the velocity, the channel gradients also show the same trend as the centroid gradients, which signifies that the dispersive quantities we introduced here should also work on other gradient measures.

If turbulent velocity broadening is known, then, as we discussed Section 5, the magnetic field strength can be obtained. However, by itself,  $M_A$  is a key parameter describing astrophysical turbulence and therefore determining its distribution is essential for many astrophysical processes.

### 6.2. Improved Techniques for Gradient Calculation and Use of Interferometers

We now have obtained a set of tools developed in the VGT (González-Casanova & Lazarian 2017; Yuen & Lazarian 2017a, 2017b; Lazarian & Yuen 2018a), e.g., error estimations, wavenumber filtering, identified shocks, and gravitationally bound objects. Some of these tools have been applied to the magnetization tracing technique discussed in this paper. In particular, the noise-suppression technique proposed in Lazarian et al. (2017) is shown

 $<sup>\</sup>overline{^{19}}$  The analytical studies of Kandel et al. (2016) open a way to calculate C from first principles for the given level of turbulence, inclination angle of the mean magnetic field, and the LOS and the assumed composition of fundamental MHD modes. Incidentally, an additional modification of Equation (6) is required to account for the other types of modes that are also present in the magnetized turbulent flow.

to be effective in maintaining the established power-law relation in Figure 6. Some of these tools we apply as the technique matures. For instance, in Lazarian & Yuen (2018a) we demonstrated how the tracing of the magnetic field can be improved with velocity gradients. This approach, based on the moving-window technique, seems promising for magnetization studies.

To obtain higher-resolution maps of magnetization, it is advantageous to use interferometers. We have shown in our previous publications (e.g., Lazarian et al. 2017) that to trace the magnetic field with gradients, one can successfully use interferometers. It is important to understand that the interferometric data can be used directly, and it is not required to have all spatial frequencies to use our gradient technique. Indeed, the gradients are calculated for the smallest separations, and filtering of low spatial frequencies is recommended to increase the signal-to-noise ratio. Therefore it is not surprising that the structure of the magnetic field can be reproduced, e.g., without employing single-dish observations. It is easy to see that the same statement is true for using the techniques presented in this paper. This opens exciting perspectives for mapping the distribution of  $M_{\rm A}$  for external galaxies.

### 6.3. Studying 3D Magnetization

Velocity gradients provide a way to probe turbulence and establish the distribution of the magnetic field directions in 3D. For instance, this can be achieved by using the galactic rotation curve for atomic hydrogen of the Milky Way. For molecular clouds, different transitions from multi-molecular species (e.g., 12CO, 13CO) can provide information of magnetic field structures at different depths, suggesting that not only the directions, but also 3D magnetization can be traced by velocity gradients through stacking the magnetic field maps from molecular tracers with different optical depth. A similar idea of exploring the 3D field tomography through velocity gradients with rotation curve is explored in Gonzalez-Casanova & Lazarian (2018). Together with the CF method, the distribution of the 3D magnetic field strength can also be acquired (see Section 5).

The MHD turbulence imprints its properties on the statistics of synchrotron intensity/polarization gradients as well as on the gradients of the emission intensity. In terms of using magnetic fluctuations, sister techniques are available. They are the SIG technique (Lazarian et al. 2017) and the SPG technique (Lazarian & Yuen 2018b). These techniques have been schown to trace the magnetic field in the POS. In particular, the SPGs (Lazarian & Yuen 2018b) can recover the 3D distribution of the magnetic field directions using the effect of Faraday depolarization. Our current results of tracing  $M_A$  with the width and the top-base ratio for the gradient distribution are also applicable to the techniques using synchrotron emissions. In terms of the SPG technique, this provides another way of studying 3D magnetization. Combining the results on magnetic directions and magnetization obtained with the gradients of synchrotron and spectral lines, an unprecedented insight into the magnetic structure of the multiphase interstellar medium (ISM) can be obtained.

Intensity gradients of gas or dust emission<sup>20</sup> provide additional information about the ISM. For instance, intensity

gradients are strongly affected by shocks (see Yuen & Lazarian 2017b). This opens interesting prospects of studying shocks and sonic Mach numbers by comparing the distribution of velocity and intensity gradient orientations. We will explore this possibility elsewhere.

### 6.4. Calculating the Distribution of the Expected Dust Polarization

Magnetic field tracing is routinely done with dust polarization. It is frequently assumed that the observed polarization represents the projected magnetic field weighted by gas density. This is approximately true when two conditions are simultaneously satisfied: (1) a relatively high grain alignment (greater than a few percent) and (2) the magnetic fields in the POS do not change significantly along the LOS. While the former is mostly satisfied in the diffuse interstellar media (see Lazarian 2007 for a review), the latter is a more subtle requirement. The problem arises from the fact that the additions of the polarization and magnetic field follow different laws, which is usually underappreciated by observers. Polarization summation is a summation of quadrupole quantities, which is different from the summation of the vectors of the magnetic field. The difference becomes obvious when the directions of the magnetic field lines oscillate along the LOS.

Velocity gradients are linear vector quantities similar to those of magnetic fields. However, the addition of the gradients along the the LOS occurs in the random walk fashion due to the absence of the direction (i.e., the vector-head) of gradients by the symmetry of the anisotropic eddies. The addition method of velocity gradients is not only different from that of the magnetic field, but also for polarization. Gradients can probably better represent the projected magnetic field for the case of super-Alfvénic turbulence, i.e., when the magnetic field directions change strongly along the LOS, as both gradients and magnetic field tend to cancel themselves out, respectively.

The issue of the comparison of the gradients versus polarization as a representation of the magnetic field is an issue of our separate paper (K. H. Yuen & A. Lazarian, in preparation). Instead we provide remarks about the sub-Alfvénic case where the differences in the magnetic field direction along the LOS are limited. In this case, the variations in the measured degree of polarization reflect the variations in the magnetic field directions. These variations are also reflected by the dispersion of gradients that we studied here. By measuring this dispersion, we can therefore predict the degree of polarization expected in the given direction. In other words, at least for sub-Alfvénic turbulence, the velocity gradients can predict both the direction of the polarized radiation and the degree of polarization. This finding is important for cosmic microwave background (CMB) polarization foreground studies, where it is good to have an independent way of finding the expected polarization.

### 6.5. Comparison with Other Works

This study reveals a new valuable feature of gradients, i.e., their ability to deliver the value of magnetization through studies of the distribution of their directions within the block over which the averaging is performed. The theory of MHD turbulence predicts a distribution of wavevectors that depends on the ratio of the turbulent to magnetic energies  $\sim M_{\rm A}^2$ .

<sup>&</sup>lt;sup>20</sup> By intensity gradients we mean the measures calculated using the block-averaging procedure described in Yuen & Lazarian (2017a), and the resulting intensity gradient technique (IGT) is different from the technique using histograms of relative orientation (HRO) described in Soler et al. (2013). A comparison between the two techniques is provided in our earlier publications on gradients, as well as in our forthcoming paper containing a very detailed quantitative comparison of the IGT and the HRO.

Therefore it is only logical that we find that the distribution of the gradient orientations also depends on  $M_A$ .

This provides another way of using the information obtained with the gradient technique in order to study the properties of the magnetized ISM. Our earlier studies (e.g., Yuen & Lazarian 2017a; Lazarian & Yuen 2018a) provided ways of magnetic field tracing with the block-averaged velocity gradient orientations as well as of obtaining the sonic Mach number  $M_s$  via studying the gradient amplitudes (Yuen et al. 2018b). Therefore, combined with the results of this paper, the study of velocity gradients can provide both  $M_A$ ,  $M_S$  and the magnetic field direction. These quantities can be studied not only in 2D, but also in 3D. This brings magnetic field studies to a new level.

We would like to emphasize that what we suggest here should not be confused with the studies of the HRO technique in Soler et al. (2013) and subsequent works (e.g., Planck Collaboration et al. 2016). In this paper we discuss the distribution of the orientation of the velocity gradient orientations around the block-averaged direction (Yuen & Lazarian 2017a) of the velocity gradient. The block-averaged direction in our technique determines the magnetic field orientation. Conversel, the HRO (a) it is not capable of tracing the magnetic field direction, it relies on polarimetry to do this, (b) it uses density gradients, not velocity gradients, and (c) it is not capable of revealing  $M_A$  and  $M_s$ . The value of the HRO is obtaining the statistical correlation of the averaged density gradient orientation and the magnetic field as a function of the column density. All in all, HRO is a different technique that is introduced with a different purpose. As we mentioned earlier, our approaches of block averaging are applicable to density gradients, and this is the basis of our IGT. In terms of its comparison with the HRO, it does not have the difference given by item (b), while in terms of item (c), our research shows that in addition to being sensitive to  $M_A$  and  $M_S$ , the IGT can identify shocks. The use of the IGT and velocity gradients is synergistic as it helps revealing the regions of gravitational collapse (Yuen & Lazarian 2017b; Lazarian & Yuen 2018a).

### 7. Summary

Thist paper establishes a new way to study the ISM magnetization. We characterize the magnetization by the Alfvén Mach number  $M_A$ , the value of which is important for solving many astrophysical problems. To find  $M_A$ , we use the distribution properties of the gradient orientations, namely, the velocity gradient dispersion and the top-base ratio obtained through Gaussian fitting of the distribution (Yuen & Lazarian 2017a). We summarize our results below.

- 1. We establish the power-law relations between the statistical parameters of the distribution of gradient orientations, i.e., the variance 1 R and the top-base ratio, to the Alfvénic Mach number  $M_A$  (Section 4).
- 2. We discuss the possibility of using the galactic rotation curve and different spectral lines to obtain the 3D map of the  $M_A$  distribution.
- 3. We show that by combining  $M_A$  with the dispersion of the Doppler-broadened spectral line, we can acquire the magnetic field strength without using polarimetry.

- 4. Our method is consistent with the method of CFA in tracing  $M_A$  (Section B). We show that the gradient technique can provide maps of  $M_A$  with higher resolution.
- 5. We show that our technique of  $M_A$  tracing is a robust tool in the presence of noise (Section 4.4).
- 6. We applied our technique to H I observational data (Section 4.5) to obtain the distribution of  $M_A$  over an extensive region of the sky.
- 7. Our approach for finding  $M_A$  using the dispersion of gradient distribution is applicable not only to velocity gradients, but also to magnetic gradients that are measured with SIGs and SPGs (see Lazarian et al. 2017; Lazarian & Yuen 2018a, 2018b).

We thank Susan Clark for providing us with the H I data and friendly discussions. This publication uses data from the Galactic ALFA H I (GALFA-H I) survey data set obtained with the Arecibo L-band Feed Array (ALFA) on the Arecibo 305 m telescope. The Arecibo Observatory is operated by SRI International under a cooperative agreement with the National Science Foundation (AST-1100968), and in alliance with Ana G. Mendez-Universidad Metropolitana, and the Universities Space Research Association. The GALFA-H I surveys have been funded by the NSF through grants to Columbia University, the University of Wisconsin, and the University of California. A.L. acknowledges the support from grant NSF DMS 1622353 and ACI 1713782. We thank the anonymous referee for providing extensive important comments and suggestions on our work.

### Appendix A Gradients for Sub- and Super-Alfvénic Turbulence

In the main text we described the case of trans-Alfvénic turbulence corresponding to the injection of energy at the scale  $L_{\rm inj}$  with  $V_L = V_{\rm A}$ . If the energy is injected with the injection velocity  $V_L$  that is slower than the Alfvén speed  $V_{\rm A}$ , the turbulence is sub-Alfvénic. In the opposite case it is super-Alfvénic. The illustration of turbulence scalings for different regimes can be found in Table 3. We briefly describe the regimes below. A more extensive discussion can be found in the review by Brandenburg & Lazarian (2013).

### A.1. Sub-Alfvénic Turbulence

In the case of  $V_L < V_A$ , the Alfvénic Mach number is smaller than unity, i.e.,  $M_A = V_L/V_A < 1$ . The turbulence in the range from the injection scale  $L_{\rm inj}$  to the transition scale

$$l_{\rm trans} = L_{\rm inj} M_{\rm A}^2 \tag{7}$$

is termed weak Alfvénic turbulence. This type of turbulence means that the  $l_{\parallel}$  scale stays the same while the velocities change as  $v_{\perp} \approx V_L (l_{\perp}/L_{\rm inj})^{1/2}$  (LV99; Galtier et al. 2000). The cascading results in the change of the perpendicular scale of eddies  $l_{\perp}$  only. With the decrease of  $l_{\perp}$ , the turbulent velocities  $v_{\perp}$  decrease. Nevertheless, rather counterintuitively, the strength of the nonlinear interactions of the Alfvénic wave packets increases (see Lazarian 2016 for the description of the interaction in terms of wave packets). Eventually, at the scale  $l_{\rm trans}$ , the turbulence transforms into the strong regime, which obeys the GS95 critical balance.

From the point of view of our gradient technique, the Alfvénic perturbations are perpendicular to the magnetic field.

<sup>&</sup>lt;sup>21</sup> We would like to stress that similar results can be obtained with synchrotron intensity and SPGs techniques.

Table 3
Regimes and Ranges of MHD Turbulence

Type of MHD Turbulence	Injection Velocity	Range of Scales	Motion Type	Ways of Study
Weak	$V_L < V_A$	$[L_{\rm inj},l_{\rm trans}]$	wave-like	analytical
Strong sub-Alfvénic	$V_L < V_{ m A}$	$[l_{\rm trans},l_{ m diss}]$	eddy-like	numerical
Strong super-Alfvénic	$V_L > V_{ m A}$	$[l_{\mathrm{A}},l_{\mathrm{min}}]$	eddy-like	numerical

**Note.**  $L_{\rm inj}$  and  $l_{\rm diss}$  are injection and dissipation scales,  $M_{\rm A} \equiv u_L/V_{\rm A}$ ,  $l_{\rm trans} = L_{\rm inj} M_{\rm A}^2$  for  $M_{\rm A} < 1$  and  $l_a = L_{\rm inj} M_{\rm A}^{-3}$  for  $M_{\rm A} > 1$ , respectively.

The slow modes (see below) are sheared by Alfvénic perturbations and also create gradients perpendicular to the magnetic field. This statement is relevant both to velocity and density gradients.

The situations when the  $l_{\rm trans}$  is smaller than the turbulence dissipation scale  $l_{\rm diss}$  requires an  $M_{\rm A}$  that is unrealistically small for typical ISM conditions. Therefore, the ISM turbulence typically transits to the strong regime. If the telescope resolution is enough to resolve scales smaller than  $l_{\rm trans}$ , it is strong MHD turbulence that we make use of within our gradient technique.

The anisotropy of the eddies for sub-Alfvénic turbulence is higher than in the case of trans-Alfvénic turbulence described by GS95. The following expression was derived in LV99:

$$l_{\parallel} \approx L_{\rm inj} \left(\frac{l_{\perp}}{L_{\rm inj}}\right)^{2/3} M_{\rm A}^{-4/3},$$
 (8)

where  $l_{\parallel}$  and  $l_{\perp}$  are given in the local system of reference. For  $M_{\rm A}=1$ , one returns to the GS95 scaling. The turbulent motions at scales smaller than  $l_{\rm trans}$  obey

$$v_{\perp} = V_L \left(\frac{l_{\perp}}{L_{\rm ini}}\right)^{1/3} M_{\rm A}^{1/3},$$
 (9)

i.e., they demonstrate a Kolmogorov-type cascade perpendicular to the local magnetic field.

In the range of  $[L_{\rm inj}, l_{\rm trans}]$ , the direction of magnetic field is weakly perturbed and the local and global systems of reference are identical. Therefore the velocity gradients calculated at scales larger than  $l_{\rm trans}$  are perpendicular to the large-scale magnetic field, while at scales smaller than  $l_{\rm trans}$ , the velocity gradients follow the direction of the local magnetic fields, similar to the case of trans-Alfvénic turbulence that we discuss in the main text.

### A.2. Super-Alfvénic Turbulence

If  $V_L > V_A$ , at large scales magnetic back-reaction is not important, and up to the scale

$$l_{\mathbf{A}} = L_{\mathbf{inj}} M_{\mathbf{A}}^{-3},\tag{10}$$

the turbulent cascade is essentially a hydrodynamic Kolmogorov cascade. At the scale  $l_A$ , the turbulence transfers to the sub-Alfvénic turbulence described by GS95 scalings, i.e., an

anisotropy of the turbulent eddies starts to occur at scales smaller than  $l_{\rm A}$ .

The velocity gradients in the range from the injection scale  $L_{\rm inj}$  to  $l_{\rm A}$  are determined by hydrodynamic motions and therefore are not sensitive to the magnetic field. The contribution from these scales is better removed using spatial filtering. For scales smaller than  $l_A$ , the gradients reveal the local direction of magnetic field, as we described, e.g., in Yuen & Lazarian (2017b) and Lazarian et al. (2017), and we also discussed in the main text. For our numerical testing we are limited in the range of  $M_A > 1$  that we can employ. In the case when  $M_A$  is sufficiently small, the scale  $l_A$  is comparable to the dissipation scale  $l_{\rm dis}$  and therefore the inertial range will be entirely eliminated. Thus we have to limit our numerical testing to  $M_A < 2$ . From the theoretical point of view, there are no limitations for tracing the magnetic field within super-Alfvénic turbulence provided that the telescope or interferometer employed resolves scales smaller than  $l_A$  and  $l_A > l_{dis}$ .

### A.3. Cascades of Fast and Slow MHD Modes

In compressible turbulence, in addition to Alfvénic motions, slow and fast fundamental motion modes are present (see Biskamp 2003). These are compressible modes, and their basic properties are described, e.g., in Brandenburg & Lazarian (2013).

In short, the three modes, Alfvén, slow, and fast, have their own cascades (see Lithwick & Goldreich 2001; Cho & Lazarian 2002, 2003). Alfvénic eddy motions shear density perturbations coresponding to the slow modes and imprint their structure on the slow modes. Therefore the anisotropy of the slow modes mimics the anisotropy of Alfvén modes, which has been confirmed by numerical simulations for media dominated by gas pressure and by magnetic pressure (Cho & Lazarian 2003, Kowal & Lazarian 2010). Therefore both velocity and magnetic field gradients are perpendicular to the local direction of the magnetic field. This has been confirmed in numerical testing in Lazarian & Yuen (2018a).

Fast modes for media dominated by gas pressure are similar to the sound waves, while for media dominated by magnetic pressure, the waves correspond to magnetic field compressions. In the latter case, the properties of the fast-mode cascade were identified in Cho & Lazarian (2002). The gradients arising from fast modes are different from those by Alfvén and slow modes, as shown in Lazarian & Yuen (2018a). However, both theoretical considerations and numerical modeling (see Brandenburg & Lazarian 2013) indicate the subdominance of the fast-mode cascade compared to that of Alfvén and slow modes. In addition, in a realistic ISM, fast modes at small scales are subject to higher damping (see Yan & Lazarian 2004; Brunetti & Lazarian 2007). In numerical simulations (Lazarian & Yuen 2018a) the velocity gradients calculated with Alfvénic modes alone were indistinguishable from those obtained with all three modes present.

### Appendix B Comparison with the Correlation Function Anisotropy Technique

The technique of measuring  $M_A$  based on the CFA was suggested as a technique for tracing magnetic fields and determining  $M_A$  (Lazarian et al. 2002, Esquivel & Lazarian 2005, Burkhart et al. 2014, Esquivel et al. 2015). The

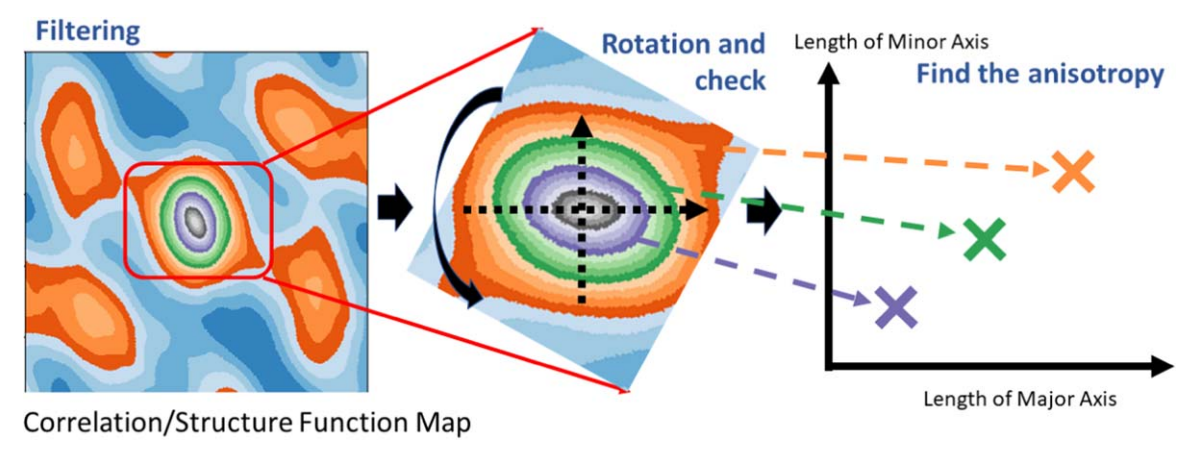


Figure 9. Illustration showing how the anisotropy direction is detected using the rotation-detection algorithm. (Left) We first locate the region having elliptical contours and place the rotation center at the origin of the ellipses. (Middle) Then we slowly rotate the contours so that we identify the major and minor axes, and both axes length are recorded for different contours. For example, the large dashed arrows shows the major and minor axes of the dark blue elliptical structure. (Right) The axes then provide the necessarily information (direction, anisotropic length) for magnetic field studies. Adapted from Yuen et al. (2018a).

advantage of using the correlation function anisotropies is that there are analytical predictions connecting the expected anisotropies with the properties of slow, fast, and Alfvén modes (Kandel et al. 2016, 2017a, 2017b). The disadvantage of the CFA compared to gradients is that the CFA requires a larger statistical area for averaging than the VGT (see Lazarian et al. 2017; Yuen & Lazarian 2017b), thus the CFA can only estimate a coarse structure of the magnetic field.

As recently reported in Yuen et al. (2018b), it is possible to use the CFA technique to trace the magnetic field direction. The (second-order) correlation function for the velocity centroid is defined as

$$CF_{2:\text{centroid}}(\mathbf{R}) = \langle \text{Ce}(\mathbf{r})\text{Ce}(\mathbf{r} + \mathbf{R}) \rangle.$$
 (11)

The direction of the major axis of the correlation function determines how the average magnetic field in the region is oriented. We would adopt the strategy as in Yuen et al. (2018a) through a fast-Fourier transform:

$$CF_{2:\text{centroid}}(\mathbf{R}) = \mathfrak{F}^{-1}\{|\mathfrak{F}\{\text{Ce}\}|^2\},\tag{12}$$

where  $\mathfrak{F}$  is the Fourier transform operator. With the correlation function computed, we can then adopt the contour-searching method as discussed in Yuen et al. (2018a). We here briefly explain their method using the cartoon from Yuen et al. (2018a) as Figure 9 here.

Figure 9 shows how the anisotropy direction can be located given a specific correlation map or structure function map. Concretely, the algorithm plots the contour lines of the map and detects the orientation of the elongated major and minor axes of each (elliptical) contour line. Then the map is rotated such that the major axis of the inner contour is parallel to the horizontal direction. The anisotropy direction is then determined from the direction of the major axis of the dark blue contour, as shown in the middle panel of Figure 9. The right panel of Figure 9 shows the axis anisotropy plot for different contours. The mean direction of the major axis orientation determines the predicted magnetic field direction using the CFA technique.

For our analysis, we compute the correlation function for the whole centroid map. In Figure 4 we compare the  $\sigma_{GD}$  and top-base ratio to the CFA axis ratio in a number of numerical cubes with different  $M_A$ . The CFA axis ratio has the similar trend with respect to  $M_A$  as the top-base ratio and the variance. However, Yuen et al. (2018a) showed that the CFA method only works

when the sampling area is about  $100^2$  out of  $792^2$ , which limits the applicability of using the CFA to obtain  $M_A$ , even though the method is well studied (Esquivel & Lazarian 2005; Esquivel et al. 2015; Kandel et al. 2017a, 2017b). In contrast, the gradient technique, including the dispersion method in this work, requires a smaller sampling area for a statistically significant result. The distribution of gradient orientation parameters (variance, topbase ratio) is therefore advantageous when observers desire an estimate of the magnetic field strength compared to the CFA method through substituting the dispersion of polarization angles in the Davis—Chandrasekhar—Fermi technique (Davis 1951; Chandrasekhar & Fermi 1953) to the dispersion of CFA orientations in the region of interest.

## Appendix C Obtaining $M_A$ by Studying the Polarization Degree

To understand why there is a kink in Figures 5 and 6 at around  $M_{\rm A}\sim 1$ , we compare our result with the Chandrasekhar–Fermi method (CF; see Chandrasekhar & Fermi 1953) with a slight modification: We compute the standard deviation of the polarization percentage  $\sigma_{\rm pol}$ % and compare it with  $M_{\rm A}$  using a number of simulation cubes that we used in our previous studies (Yuen & Lazarian 2017a, 2017b; Lazarian & Yuen 2018a). From Falceta-Gonçalves et al. (2008) we know that the traditional formulation of the CF method does not work when  $M_{\rm A}$  is close to unity. Instead, Falceta-Gonçalves et al. (2008) suggested the a straightforward generalization of the traditional relation  $\delta$  tan  $\theta_{\rm pol} \propto M_{\rm A}$ , where  $\delta\theta_{\rm pol}$  is the dispersion of the distribution of the polarization angles.

When we sample a magnetic field over an LOS scale  $\mathcal{L}$  much larger than the turbulence injection scale, an additional factor is introduced in Cho & Yoo (2016) to compensate for the contributions from multiple LOS eddies in their modification of the Davis–Chandrasekhar–Fermi (Davis 1951; Chandrasekhar & Fermi 1953) technique:

$$\alpha = \sqrt{\frac{L}{\mathcal{L}}},\tag{13}$$

which increases the relative importance of the observed mean magnetic field compared to the random magnetic field. Indeed, the integration of the fluctuating magnetic field along the LOS is a random walk process with the integral  $\sim \sqrt{LL}$ , while the contribution of mean field increases as  $\sim L$ . Therefore the ratio of the  $\int \delta B ds / \int B_0 ds \approx M_{\rm A} \alpha$ . This is the ratio that is available from observations. Thus we adopt

$$\delta \tan \theta_{\rm pol} \approx \delta \theta_{\rm pol} \propto \alpha M_{\rm A},$$
 (14)

where we assumed small angle variations. It is important for us is that  $P_{\%} = \sqrt{Q^2 + U^2}/I$  is proportional to the difference of cross sections  $C_x - C_y$  (see Lee & Draine 1985 for a detailed discussion), where I, Q, U are the Stokes parameters. The fluctuation of  $P_{\%}$ , i.e.,  $\delta P_{\%} = P_{\%} - \langle P_{\%} \rangle$ , can be obtained assuming that fluctuations in angle are measured from the mean field direction. Thus for  $\theta \ll 1$ ,  $\delta P_{\%} \sim (\delta \theta_{\rm pol})^2$  and the squared dispersion of polarization

$$\sigma_{\text{pol}\%}^2 = \langle (\delta P\%)^2 \rangle \sim (\delta \theta_{\text{pol}})^4,$$
 (15)

which means that

$$\sigma_{\text{pol}\%} \sim M_{\text{A}}^2 \alpha^2.$$
 (16)

Therefore  $\sigma_{\rm pol\%} \sim \delta\theta_{\rm pol}^2$ , we expect a  $M_{\rm A}^2$  dependence for small  $M_{\rm A}$ . The right panel of Figure 5 shows the plot of  $\sigma_{\rm pol\%} - M_{\rm A}$  using the simulations from LY18. The result in Figure 5 is equivalent to the modified CF method in F08.

For our numerical study  $\alpha \approx 1$ , and we did not explore the dependence  $^{22}$  of  $\sigma_{\text{pol}\%}$  on  $\alpha$ . Instead, by using more than 30 numerical cubes with different  $M_S$ ,  $M_A$  and resolutions, Figure 5 shows that there is a power-law relation of  $\sigma_{\text{pol}\%} \propto M_A^2$  at  $M_A < 1$ . The flattered fitting line with  $M_A \in [1, 2]$  has a proportionality of  $\sigma_{\text{pol}\%} \propto M_A^{0.6}$ . For gradient dispersion, the power law becomes  $(1 - R) \propto M_A^{0.06}$ . The ratio of the power-law index and also the behavior in the two regimes of  $M_A$  are similar for the gradient dispersion method and the CF method. This analysis suffices to show that the gradient dispersion technique can estimate the magnetization of a system in a way similar to the CF method.

### **ORCID iDs**

Zekun Lu https://orcid.org/0000-0001-7961-7617

### References

Andersson, B.-G., Lazarian, A., & Vaillancourt, J. E. 2015, ARA&A, 53, 501
Ballesteros-Paredes, J., Klessen, R. S., Mac Low, M.-M., & Vazquez-Semadeni, E. 2007, in Protostars and Planets V, ed. B. Reipurth, D. Jewitt, & K. Keil (Tucson, AZ: Univ. Arizona Press), 63

Bell, A. R. 1978, MNRAS, 182, 147

Biskamp, D. 2003, Magnetohydrodynamic Turbulence (Cambridge: Cambridge Univ. Press)

Bourke, T. L., Myers, P. C., Robinson, G., & Hyland, A. R. 2001, ApJ, 554, 916

Brandenburg, A., & Lazarian, A. 2013, SSRv, 178, 163

Brunetti, G., & Lazarian, A. 2007, MNRAS, 378, 245

Burkhart, B. 2018, ApJ, submitted (arXiv:1801.05428)

Burkhart, B., Collins, D. C., & Lazarian, A. 2015, ApJ, 808, 48

Burkhart, B., & Lazarian, A. 2012, ApJL, 755, L19

Burkhart, B., Lazarian, A., Leão, I. C., de Medeiros, J. R., & Esquivel, A. 2014, ApJ, 790, 130

```
Caprioli, D., & Spitkovsky, A. 2014, ApJ, 783, 91
Chandrasekhar, S., & Fermi, E. 1953, ApJ, 118, 113
Chapman, N. L., Davidson, J. A., Goldsmith, P. F., et al. 2013, ApJ, 770, 151
Chen, C.-Y., King, P. K., & Li, Z.-Y. 2016, ApJ, 829, 84
Chepurnov, A., & Lazarian, A. 2009, ApJ, 693, 1074
Chitsazzadeh, S., Houde, M., Hildebrand, R. H., & Vaillancourt, J. 2012, ApJ,
  749, 45
Cho, J., & Lazarian, A. 2002, PhRvL, 88, 245001
Cho, J., & Lazarian, A. 2003, MNRAS, 345, 325
Cho, J., Lazarian, A., & Vishniac, E. T. 2002a, ApJ, 564, 291
Cho, J., Lazarian, A., & Vishniac, E. T. 2002b, ApJL, 566, L49
Cho, J., & Vishniac, E. T. 2000, ApJ, 539, 273
Cho, J., & Yoo, H. 2016, ApJ, 821, 21
Clark, S. E., Hill, J. C., Peek, J. E. G., Putman, M. E., & Babler, B. L. 2015,
  PhRvL, 115, 241302
Clemens, D. P., Pavel, M. D., & Cashman, L. R. 2012a, ApJS, 200, 21
Clemens, D. P., Pavel, M. D., & Cashman, L. R. 2013, AJ, 145, 74
Clemens, D. P., Pinnick, A. F., Pavel, M. D., & Taylor, B. W. 2012b, ApJS,
   200, 19
Crutcher, D. 2007, Transformational Science with ALMA: Through Disks to
   Stars and Planets (Charlottesville, VA: NRAO), 19
Crutcher, R. 2010, in From Stars to Galaxies: Connecting our Understanding of
  Star and Galaxy Formation (Gainesville, FL: Univ. Florida), 3
Crutcher, R. M. 1999, ApJ, 520, 706
Crutcher, R. M. 2012, ARA&A, 50, 29
Crutcher, R. M., Troland, T. H., Lazareff, B., Paubert, G., & Kazès, I. 1999,
    pJL, 514, L121
Cudlip, W., Furniss, I., King, K. J., & Jennings, R. E. 1982, MNRAS,
  200, 1169
Davis, L., Jr. 1951, PhRv, 81, 890
Dragovan, M. 1986, ApJ, 308, 270
Draine, B. T. 2011, Physics of the Interstellar and Intergalactic Medium
  (Princeton, NJ: Princeton Univ. Press)
Elmegreen, B. G., & Scalo, J. 2004, ARA&A, 42, 211
Esquivel, A., & Lazarian, A. 2005, ApJ, 631, 320
Esquivel, A., & Lazarian, A. 2010, ApJ, 710, 125
Esquivel, A., & Lazarian, A. 2011, ApJ, 740, 117
Esquivel, A., Lazarian, A., & Pogosyan, D. 2015, ApJ, 814, 77
Eyink, G. L., Lazarian, A., & Vishniac, E. T. 2011, ApJ, 743, 51
Falceta-Gonçalves, D., Lazarian, A., & Kowal, G. 2008, ApJ, 679, 537
Falgarone, E., Troland, T. H., Crutcher, R. M., & Paubert, G. 2008, A&A,
  487, 247
Fermi, E. 1949, PhRv, 75, 1169
Galtier, S., Nazarenko, S. V., Newell, A. C., & Pouquet, A. 2000, JPIPh,
Ginzburg, V. L., & Syrovatskii, S. I. 1964, The Origin of Cosmic Rays
  (New York: Macmillan)
Goldreich, P., & Sridhar, S. 1995, ApJ, 438, 763
González-Casanova, D. F., & Lazarian, A. 2017, ApJ, 835, 41
Gonzalez-Casanova, D. F., & Lazarian, A. 2018, ApJ, submitted (arXiv:1805.
Goodman, A. A., Crutcher, R. M., Heiles, C., Myers, P. C., & Troland, T. H.
   1989, ApJL, 338, L61
Heiles, C., Goodman, A. A., McKee, C. F., & Zweibel, E. G. 1993, in
  Protostars and Planets III, ed. E. Levy & J. I. Lunine (Tucson, AZ: Univ.
  Arizona Press), 279
Heyer, M., Gong, H., Ostriker, E., & Brunt, C. 2008, ApJ, 680, 420
Hildebrand, R. H. 1988, QJRAS, 29, 327
Hildebrand, R. H., Davidson, J. A., Dotson, J. L., et al. 2000, PASP, 112, 1215
Hildebrand, R. H., Dragovan, M., & Novak, G. 1984, ApJL, 284, L51
Hildebrand, R. H., Kirby, L., Dotson, J. L., Houde, M., & Vaillancourt, J. E.
  2009, ApJ, 696, 567
Holland, W. S., Robson, E. I., Gear, W. K., et al. 1999, MNRAS, 303, 659
Houde, M., Hull, C. L. H., Plambeck, R. L., Vaillancourt, J. E., &
  Hildebrand, R. H. 2016, ApJ, 820, 38
Houde, M., Rao, R., Vaillancourt, J. E., & Hildebrand, R. H. 2011, ApJ,
Houde, M., Vaillancourt, J. E., Hildebrand, R. H., Chitsazzadeh, S., &
   Kirby, L. 2009, ApJ, 706, 1504
Hull, C. L. H., Mocz, P., & Burkhart, B. 2017, ApJL, 842, L9
Hull, C. L. H., Plambeck, R. L., Bolatto, A. D., et al. 2013, ApJ, 768, 159
Jokipii, J. R. 1966, ApJ, 146, 480
Kandel, D., Lazarian, A., & Pogosyan, D. 2016, MNRAS, 461, 1227
Kandel, D., Lazarian, A., & Pogosyan, D. 2017a, MNRAS, 464, 3617
Kandel, D., Lazarian, A., & Pogosyan, D. 2017b, MNRAS, 470, 3103
Kennicutt, R. C., Jr. 1998a, ApJ, 498, 541
```

Kennicutt, R. C., Jr. 1998b, ARA&A, 36, 189

 $<sup>\</sup>overline{^{22}}$  The dependence of  $\sigma_{\text{pol}\%}$  on  $\alpha$  is different from the dependence of the dispersion of the velocity gradients on  $\alpha$ . The latter does not depend on the LOS integration and therefore is independent of  $\alpha$ . Therefore, by finding the  $M_{\text{A}}$  using the two approaches, ee can find the important physical parameter of the turbulent volume  $L/\mathcal{L}$ .

```
Koenigl, A. 1991, ApJL, 370, L39
Kowal, G., & Lazarian, A. 2010, ApJ, 720, 742
Kowal, G., Lazarian, A., & Beresnyak, A. 2007, ApJ, 658, 423
Larson, R. B. 1981, MNRAS, 194, 809
Lazarian, A. 2006, ApJL, 645, L25
Lazarian, A. 2007, JQSRT, 106, 225
Lazarian, A. 2016, ApJ, 833, 131
Lazarian, A., & Esquivel, A. 2003, ApJL, 592, L37
Lazarian, A., & Pogosyan, D. 2000, ApJ, 537, 720
Lazarian, A., & Pogosyan, D. 2004, ApJ, 616, 943
Lazarian, A., & Pogosyan, D. 2012, ApJ, 747, 5
Lazarian, A., & Pogosyan, D. 2016, ApJ, 818, 178
Lazarian, A., Pogosyan, D., & Esquivel, A. 2002, in ASP Conf. 276, Seeing
   Through the Dust: The Detection of H I and the Exploration of the ISM in
   Galaxies, ed. A. R. Taylor, T. L. Landecker, & A. G. Willis (San Francisco,
   CA: ASP), 182
Lazarian, A., & Vishniac, E. T. 1999, ApJ, 517, 700
Lazarian, A., & Yan, H. 2014, ApJ, 784, 38
Lazarian, A., & Yuen, K. H. 2018a, ApJ, 853, 96
Lazarian, A., & Yuen, K. H. 2018b, ApJ, in press (arXiv:1802.00028)
Lazarian, A., Yuen, K. H., Lee, H., & Cho, J. 2017, ApJ, 842, 30
Lee, H. M., & Draine, B. T. 1985, ApJ, 290, 211
Lithwick, Y., & Goldreich, P. 2001, ApJ, 562, 279
Mac Low, M.-M., & Klessen, R. S. 2004, RvMP, 76, 125
Maron, J., & Goldreich, P. 2001, ApJ, 554, 1175
McKee, C. F., & Ostriker, E. C. 2007, ARA&A, 45, 565
Mestel, L., & Spitzer, L., Jr. 1956, MNRAS, 116, 503
```

```
Mouschovias, T. C., & Spitzer, L., Jr. 1976, ApJ, 210, 326
Novak, G., Dotson, J. L., Dowell, C. D., et al. 1997, ApJ, 487, 320
Parker, E. N. 1965, ApJ, 142, 584
Parker, E. N. 1979, Cosmical Magnetic Fields: Their Origin and Their Activity
  (Oxford: Clarendon)
Peek, J. E. G., Babler, B. L., Zheng, Y., et al. 2018, ApJS, 234, 2
Planck Collaboration, Ade, P. A. R., Aghanim, N., et al. 2015, A&A,
  576, A104
Planck Collaboration, Ade, P. A. R., Aghanim, N., et al. 2016, A&A,
  586, A138
Schmidt, M. 1959, ApJ, 129, 243
Shu, F. H. 1977, ApJ, 214, 488
Shu, F. H. 1992, The Physics of Astrophysics. Volume II: Gas Dynamics (Mill
   Valley, CA: Univ. Science Books)
Shu, F., Najita, J., Ostriker, E., et al. 1994, ApJ, 429, 781
Soler, J. D., Hennebelle, P., Martin, P. G., et al. 2013, ApJ, 774, 128
Vaillancourt, J. E., & Matthews, B. C. 2012, ApJS, 201, 13
Xu, S., & Lazarian, A. 2018, ApJ, submitted (arXiv:1802.00987)
Yan, H., & Lazarian, A. 2002, PhRvL, 89, 281102
Yan, H., & Lazarian, A. 2004, ApJ, 614, 757
Yoo, H., & Cho, J. 2014, ApJ, 780, 99
Yuen, K. H., Chen, J., Hu, Y., et al. 2018a, ApJ, in press (arXiv:1804.02732)
Yuen, K. H., & Lazarian, A. 2017a, ApJL, 837, L24
Yuen, K. H., & Lazarian, A. 2017b, ApJ, submitted (arXiv:1703.03026)
Yuen, K. H., Lazarian, V., & Lazarian, A. 2018b, ApJL, submitted (arXiv:1802.
  00024)
Zuckerman, B., & Palmer, P. 1974, ARA&A, 12, 279
```